

CHARACTERIZATION OF EXOPLANET ATMOSPHERES WITH THE OPTICAL CORONAGRAPH ON WFIRST

B. LACY,¹ D. SHLIVKO,² AND A. BURROWS¹¹*Department of Astrophysics, Princeton, NJ, 08540*²*California Institute of Technology, Pasadena, CA, 91125*

ABSTRACT

WFIRST-CGI will obtain images and low-resolution spectra of a handful to a dozen extrasolar planets and protoplanetary disks. Its unprecedented contrast levels in the optical will provide astronomers' first direct look at mature, Jupiter-sized planets at moderate separations. This paper addresses the question: what science can be done with such data? An analytic noise model, informed by recent engineering developments, is used to compute maximum achievable signal-to-noise ratios and scientifically viable integration times for hypothetical star-planet systems, as well as to investigate the constraining power of various combinations of WFIRST-CGI photometric and spectral observations. This work introduces two simple models for planetary geometric albedos inspired largely by Solar System gas giants. The first planet model is a hybrid Jupiter-Neptune model, which separately treats the short and long wavelengths where chromophores and methane dominate absorption, respectively. The second planet model fixes cloud and haze properties in *CoolTLusty* to match Jupiter's albedo spectrum, then perturbs the metallicity between 1 and 30 times solar. MCMC retrievals performed on simulated observations are used to assess the precision with which planet model parameters can be measured subject to different exposure times and observing cases.

Keywords: exoplanets, direct-imaging, WFIRST-AFTA, WFIRST-CGI

1. INTRODUCTION

Space-based high-contrast imaging promises to inaugurate the next phase of exoplanet atmospheric studies. Initial efforts from the ground have successfully imaged young self-luminous, wide-separation exoplanets (and brown dwarfs) in the infrared, where planet-star contrast ratios are on the order of $10^{-4/5}$, (GPI: [Macintosh et al. 2006](#); SPHERE: [Mesa et al. 2015](#)). NASA’s Wide-Field Infrared Survey Telescope (WFIRST)/Astrophysics Focused Telescope Assets (AFTA) mission is likely to fly an optical coronagraph (CGI) capable of detecting and characterizing cool giant exoplanets (EGP’s) around nearby stars at separations of ~ 1 to ~ 6 AU, where contrast ratios are on the order of 10^{-9} ([Spergel et al. 2013](#)). WFIRST-CGI is defined as a technology development mission, so simply attaining the specified contrasts and instrument capabilities constitutes mission success. It is nonetheless an exciting opportunity to obtain images and low-resolution optical albedo spectra at unprecedented contrast ratios. This advance in observational capability raises the theoretical question: what new insights into giant planets can be gleaned from such data? The optical range can be a powerful tool for probing giant exoplanet characteristics. It spans prominent methane features near $\sim 0.62 \mu\text{m}$, $\sim 0.74 \mu\text{m}$, $\sim 0.81 \mu\text{m}$, and $\sim 0.89 \mu\text{m}$, ammonia features at $\sim 0.65 \mu\text{m}$ and $\sim 0.79 \mu\text{m}$, and a broad water band at $\sim 0.94 \mu\text{m}$. In addition, Rayleigh scattering off molecules and Mie-like scattering off cloud particulates and hazes can modify planet reflectivity in diagnostic ways ([Burrows et al. 2004](#); [Sudarsky et al. 2005](#)). As the design process converges, it is timely to consider the degree to which WFIRST-CGI low-resolution spectra and imaging will be able to probe these anticipated spectral signatures.

A number of studies have already begun to explore the expected capabilities of WFIRST-CGI. These studies build on well-established reflection spectra theory ([Marley et al. 1999](#); [Sudarsky et al. 2000](#)), the literature surrounding the viability of space-based coronagraph or external occulter surveys ([Agol 2007](#); [Brown & Soummer 2010](#); [Savransky et al. 2010](#); [Turnbull et al. 2012](#); [Stark et al. 2014](#)), and the ongoing engineering efforts to design and build space-based external occulters and coronagraphs in general and for WFIRST-CGI specifically ([Kasdin et al. 2003](#); [Soummer 2005](#); [Carlotti et al. 2011](#); [Cady et al. 2016](#); [Krist et al. 2016](#); [Zimmerman et al. 2015](#); [Balasubramanian et al. 2016](#)). Much work has gone into estimating the yield of the imaging portion of the mission. [Greco & Burrows \(2015\)](#) performed Monte Carlo simulations to quantify the detectability of giant planets under various conditions in the context of WFIRST, (see also [Savransky & Garrett 2016](#); [Garrett et al. 2017](#); [Traub et al. 2016](#)). Many quantitative predictions of yields in these studies depend upon assumptions of instrument performance and extrapolations of underlying exoplanet populations into regimes for which we do not yet have sufficient data. Explorations of the integral field spectrograph (IFS) capabilities are thus understandably lagging behind imaging, since they require additional assumptions about likely planet atmospheres. [Cahoy et al. \(2010\)](#) studied how optical reflection spectra and colors vary with planet/star separation, metallicity, mass, and observed phase. [Lupu et al. \(2016\)](#) developed an atmospheric retrieval methodology for optical reflection spectra and demonstrated its abilities on simulated direct imaging data. Their geometric albedo models allowed for one or two cloud layers, variations in surface gravity, and variations in methane abundance. [Robinson et al. \(2016\)](#) presented a general model for any space-based coronagraph equipped with an IFS and computed the required integration times to reach a given signal-to-noise ratio (SNR) as a function of host star effective temperature and wavelength for a variety of planet characteristics. [Nayak et al. \(2017\)](#) used the noise model of [Robinson et al. \(2016\)](#) to simulate WFIRST-CGI data and extended the work of [Lupu et al.](#)

(2016) to consider how uncertainties in planet radius and orbital phase influence their ability to fit similar models. Since the design process has continued, assumptions made in Robinson et al. (2016) and Nayak et al. (2017) can now be improved. Nemati et al. (2017) present an analytic parameterized noise model tailored particularly to WFIRST-CGI observations, utilizing the latest available instrument specifications and exploring how mission performance depends on these instrument specifications. Their particular focus was on raw contrast, post-processing, and core throughput. Rizzo et al. (2017) recently conducted a rigorous simulation of the IFS + EMCCD performance publicly available. Their software `crispy` takes a high-resolution astrophysical-observing-scenario-dependent datacube as input and then outputs a datacube consistent with the WFIRST-CGI data products. These resulting datacubes can then be used to test post-processing methods, observing scenarios, and instrumental parameters, all in the effort to optimize the science yield of the mission.

In this paper, we create a versatile pipeline to simulate WFIRST-CGI observations which can be adapted to explore new planet models and target system geometries, and can be updated with the latest expected instrument capabilities as they are finalized. The low resolution and low throughput of the WFIRST-CGI IFS will yield data unlikely to constrain detailed atmosphere models. We thus present two appropriately simple planet models as input for our pipeline: a hybrid Jupiter-Neptune albedo spectrum, and a suite of reflection spectra generated with *CoolThrusty* (Hubeny & Lanz 1995; Sudarsky et al. 2003; Burrows et al. 2006) which fix cloud parameters tuned to match Jupiter at a metallicity of 0.5 dex (around $3.16 \times$ solar), and then perturb the metallicity between 1 and 30 times solar. Both classes of geometric albedo model are paired with Jupiter’s measured phase function (Mayorga et al. 2016). Rather than utilizing the detailed model of Rizzo et al. (2017) in our pipeline, we chose to adopt the noise model of Nemati et al. (2017) to simulate observed spectra. We then carry out MCMC parameter retrievals to assess the recovery of underlying planet model parameters. This allows us to quickly explore many variations of our planet models, many planet-star scenarios, and compare results for several combinations of WFIRST-CGI’s imaging and spectral coverage.

In section 2, we provide a brief review of the portions of reflection spectra theory most relevant to simulating and interpreting direct images of exoplanets. Section 3 outlines the WFIRST-CGI noise model implemented in our pipeline, with detailed calculations left to the Appendix. Section 4 describes the two planet models used as input for our pipeline. Section 5 presents calculations of integration times to achieve different *SNR*’s and parameter estimate precisions for varying *SNR*’s, integration times, and observing cases. Section 6 discusses the implications of these results for giant exoplanet science in the era of WFIRST-CGI, and section 7 summarizes our work, highlighting important conclusions.

2. RELEVANT REFLECTION SPECTRA THEORY

To investigate the relationship between a planet’s atmospheric properties and the resulting observations from a space-based telescope such as WFIRST, one must focus primarily on modeling the geometric albedo spectrum and deriving the resulting planet-star flux ratios. For mature EGP’s whose thermal emissions in the optical are negligible, the emergent flux from the planet comes almost entirely from reflection of stellar light. Thus, the wavelength-dependent planet-star flux ratio is merely the fraction of stellar light reflected toward the observer by the EGP. This depends trivially on the planet’s size and orbital distance, but is also a more intricate function of the planet’s phase and atmospheric composition.

In addition to these orbital and physical determinants of the flux ratio spectrum, some systems may present themselves with a number of more exotic and subtle factors which are not presently reflected in our models. For instance, additional dependencies on orbital inclination may arise from the presence of rings, which for Saturn can vary its luminosity by up to a factor of two (Mallama 2012), or from rotation-induced oblateness (Mallama et al. 2017), which influences brightness according to the area oriented to reflect light toward Earth. Latitudinal variations in atmospheric composition (Mallama et al. 2017; Schmude et al. 2015) may add further to this inclination dependence. Other corrections may be needed to account for intrinsic temporal brightness variations due to rotation and/or evolution of atmospheric structure, as is seen for Neptune (Schmude et al. 2016). Lastly, though planetary phase functions for the solar-system planets are not well known, we do know that opposition effects, glories, and rainbows are possible for a range of atmospheric and surface characteristics. We do not attempt to model or incorporate any of these possibilities, concluding that at this stage in exoplanet reflection science such detailed models are premature.

2.1. Albedos and Phase Functions

Formally, the proportion of incident light of wavelength λ reflected by a planet at a phase angle α toward an observer is governed by the planet’s geometric albedo $A_g(\lambda)$ and its phase function $\Phi(\alpha, \lambda)$, where α is the exoplanet-centric angle between the star and the observer (Sudarsky et al. 2000; Madhusudhan & Burrows 2012; Greco & Burrows 2015). The geometric albedo measures the reflectivity of the planet at full phase ($\alpha = 0$), while the phase function is normalized to 1 at full phase and dictates the variation of reflectivity with phase. In terms of these quantities, the planet-star flux ratio is given by

$$\frac{F_p}{F_\star}(\alpha, \lambda) = \frac{R_p^2}{a^2} \cdot A_g(\lambda) \cdot \Phi(\alpha, \lambda), \quad (1)$$

where R_p is the planet’s radius and a is its orbital distance.

A planet’s geometric albedo and the behavior of its phase function are determined by the scattering properties of its atmosphere, which in turn depend on the atmosphere’s composition. Cloud layers in the atmosphere provide the primary source of scattering, giving the planet a non-negligible albedo (typically on the order of a few tenths). Scattering effects from hazes and gases further increase the albedo, but their influence is less substantial. Clouds and hazes also provide sources of absorption in the atmosphere, though the effect is modest relative to that of gases. The absorption of gases is also far more wavelength-dependent than that of other atmospheric components, making gases the primary sculptors of the shape of the geometric albedo spectrum (Sudarsky et al. 2000, 2003, 2005).

The subtle dependence of a planet’s phase function $\Phi(\alpha, \lambda)$ on wavelength has important consequences for spectral observations of an exoplanet near quadrature ($\alpha=90^\circ$). At quadrature, the difference in reflectivity at different wavelengths may vary at levels comparable to variations in geometric albedo with wavelength. This phenomenon is best illustrated by the phase dependence of a planet’s color indices (Sudarsky et al. 2005; Mayorga et al. 2016; Cahoy et al. 2010), which may vary by up to one magnitude (through Johnson-Cousins filters) between new and full phases for an EGP in an edge-on orbit. Figure 6 demonstrates the variation in color over an orbit in the WFIRST-CGI imaging bands.

2.2. Time-Dependent Observables

It is possible to substitute the dependencies of the planet-star flux ratio on orbital distance and phase with more standardized orbital parameters: inclination, eccentricity, argument of periastron, and time elapsed since periastron. This substitution requires a mapping that gives the planet's phase angle α as a function of time; we follow the formalism summarized in [Madhusudhan & Burrows \(2012\)](#) which draws on many previous works: [Russell \(1916\)](#); [Horak \(1950\)](#); [van de Hulst \(1974, 1981\)](#); [Seager & Sasselov \(1998\)](#); [Marley et al. \(1999\)](#); [Sudarsky et al. \(2000\)](#); [Seager et al. \(2000\)](#); [Stam et al. \(2004\)](#); [Cahoy et al. \(2010\)](#). We first calculate the planet's mean anomaly M from its definition:

$$M = 2\pi \cdot \frac{t}{P}, \quad (2)$$

where t is the time since periastron and P is the period. Next, to determine the exoplanet's eccentric anomaly, E , we utilize the following relationship:

$$M = E + e \cdot \sin(E), \quad (3)$$

where e is the orbit's eccentricity. Note that because M increases monotonically with E ($\frac{dM}{dE} = 1 + e \cdot \cos(E)$ and $0 \leq e < 1$), there will always exist a unique solution for E . The true anomaly θ is then related to the eccentric anomaly via

$$\theta = 2 \cdot \tan^{-1} \left(\sqrt{\frac{1+e}{1-e}} \cdot \tan(E/2) \right). \quad (4)$$

Finally, the phase angle can be retrieved using

$$\alpha = \cos^{-1}(\sin(i) \cdot \sin(\theta + \omega_p)), \quad (5)$$

where i is the orbit's inclination (0° representing a face-on orbit) and ω_p is the argument of periastron.

Using this formalism, observables such as exoplanetary colors and planet-star flux ratios can be generated as a function of time for an orbit with known Keplerian elements. This allows one to simulate observations using measured properties of known radial velocity (RV) planets around nearby stars, the most likely targets for WFIRST-CGI ([Traub et al. 2016](#)).

3. WFIRST-CGI MISSION AND NOISE MODEL

WFIRST-CGI's coronagraph will directly image disks and exoplanets around a dozen or so nearby stars, as well as provide low-resolution spectra of several planets ([Zhao 2014](#); [Noecker et al. 2016](#)). In addition to any planets discovered by the mission, likely targets are known \sim Neptune- to \sim Jupiter-sized RV planets orbiting one to six AU around stars 3 to 50 parsecs away ([Traub et al. 2016](#)). Sensitive to cool, moderate-separation EGP's, the mission will probe the structure and composition of planetary systems unlike those best studied by transit, RV, and ground-based IR direct imaging.

To accomplish this, WFIRST-CGI will be equipped with two coronagraphs: a hybrid lyot coronagraph (HLC, [Trauger et al. 2016](#)), and a shaped-pupil coronagraph (SPC, [Balasubramanian et al. 2016](#)). At the time of writing this paper, the HLC and SPC are intended for imaging in a series of bands spanning $0.4 \mu\text{m}$ to $1.0 \mu\text{m}$ with spectral widths ranging from 5% to 10%. The SPC will also be paired with an IFS ([Saxena et al. 2017](#)), capable of dispersing light with resolving power of $R \sim 50$ in three slightly overlapping bands spanning $0.6 \mu\text{m}$ to $1.0 \mu\text{m}$ with $\sim 18\%$ width. Both coronagraphs will be able to achieve contrast ratios on the order of 10^{-9} . Figure 1 shows a model of

the two coronagraphs performance as a function of working angle in terms of effective contrast and core throughput (Krist et al. 2016). Figure 2 shows the currently reported imaging and IFS band locations and widths¹. Precise central wavelengths and widths of these bands, as well as contrast capabilities, continue to change as the mission proceeds through the development process. The total mission budgetary constraints may dictate a scaled-back coronagraph mission with only a subset of these imaging bands and IFS filters. For this reason, we consider a variety of combinations of imaging and spectral coverage in our study of likely science capabilities.

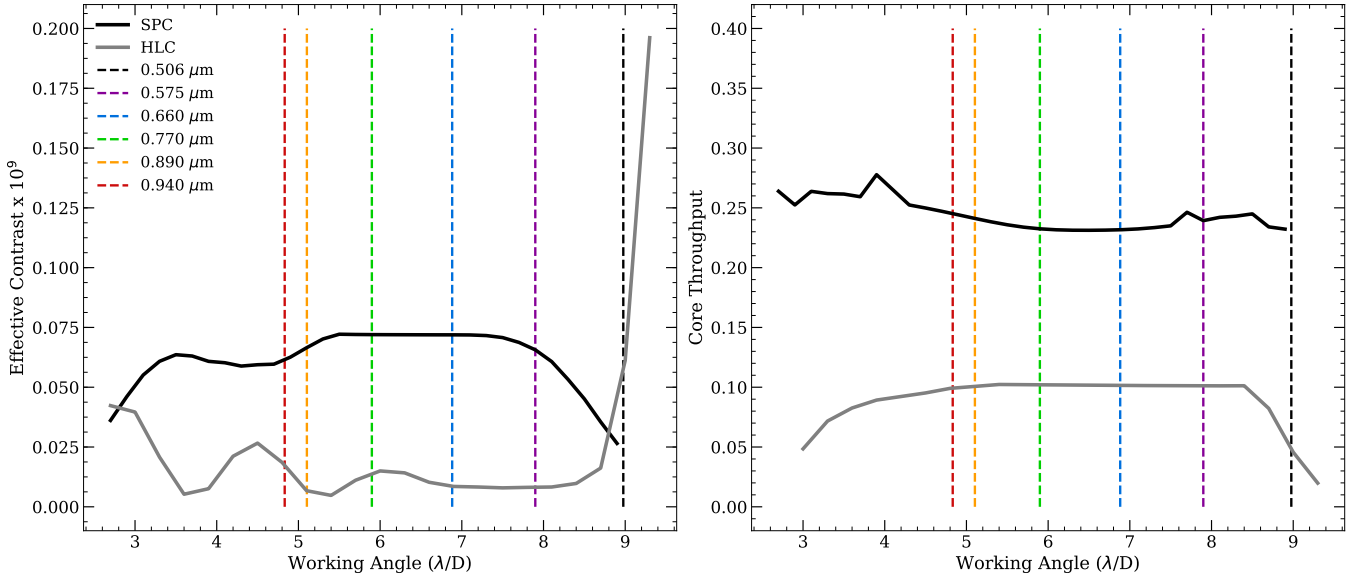


Figure 1. Modeled effective contrast and core throughput (see Appendix for precise definitions of these quantities) of the SPC and HLC over different working angles in units of λ/D . Models are taken from Krist et al. 2016. The SPC design will be used with the IFS, and the HLC design will be used for imaging. These curves can be read as wavelength-dependent performance for a given planet-star system if one converts the fixed working angle of the planet in radians into appropriate λ/D units for the wavelength of interest. The centers of the two shortest imaging bands, the three IFS bands, and the longest wavelength imaging band are marked by dashed lines for our fiducial system approximating the Jupiter-Sun system: a planet 5 AU from its primary, observed from a distance of 11 pc, at $\alpha=60^\circ$ orbital phase angle.

Due to the extremely low flux levels and long integration times under which WFIRST-CGI will operate, the e2v CCD201-20 EMCCD has been baselined as the detector for each of the instrument cameras (Harding et al. 2016). EMCCD’s can be operated in a photon-counting mode which essentially nullifies read noise (Nemati 2014; Harding et al. 2016; Denvir & Conroy 2003). To allow final data analysis with reference differential imaging (RDI, Ygouf et al. 2015), a typical observing procedure for a spectroscopic or imaging target could follow four steps (Krist et al. 2016; Nemati et al. 2017):

1. Focus on a nearby star of the same brightness and approximate color as target.
2. Focus on a nearby star significantly brighter than the target and dig the dark hole.

¹ <https://wfirst.ipac.caltech.edu/sims/Param.db.html>

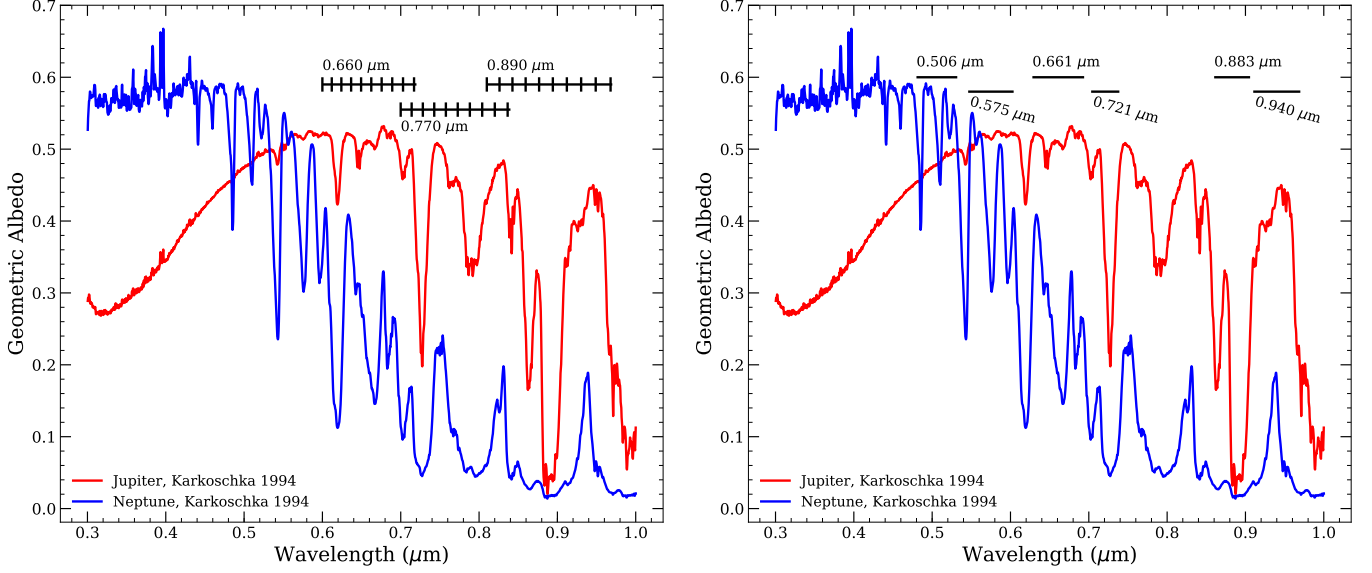


Figure 2. Wavelength coverage proposed for WFIRST-CGI IFS (left) and imaging (right) filters at the time of writing. Both are overlaid against Karkoschka (1994)’s measurements of Jupiter’s and Neptune’s geometric albedo spectra. The IFS will cover three overlapping bands: a 18.2% full-width band centered at $0.660 \mu\text{m}$, a 18.2% width band centered at $0.770 \mu\text{m}$, and a 18.0% width band centered at $0.890 \mu\text{m}$. Vertical hash marks delineate a resolution of $R = 50$ within the IFS bands. The imager will have six bands centered at: 0.506 , 0.575 , 0.661 , 0.883 , 0.721 , and $0.940 \mu\text{m}$, with corresponding widths of: 10.3%, 10.1%, 10.0%, 5.2%, 5.0%, and 6.4%, respectively. For the purposes of this work, all bands are assumed perfect top-hat functions between 0% transmission and 90% transmission.

3. Observe the target.
4. Return to the nearby star of the same brightness and color to carry out observations which will be used to remove speckles.

According to the preliminary plan presented in Traub et al. (2016), the CGI portion of the WFIRST mission will be allotted a total of 3000 hours for all engineering, imaging, and spectroscopy. Thirty of these hours will go to planet discovery direct imaging; the remaining time will go to detailed planet characterization with spectroscopy and imaging. In light of these mission lifetime constraints and the constraints placed by thermal stability of the instrument, observation of a single object exceeding 300 hours (including time on target and time calibrating) is considered infeasible.

Our noise model closely follows the work of Nemati et al. (2017), with some slight adaptations. Here, we provide a brief overview of that model. Detailed calculations of contributing noise terms, throughputs, and quantum efficiencies are included in the Appendix. Our model represents a space-based telescope with primary mirror collecting area A_{PM} equipped with a coronagraph achieving raw contrast C_{raw} , planetary, zodiacal, and speckle throughputs τ_{pla} , τ_{zod} , and τ_{spe} , and inner and outer working angles Θ_{IWA} and Θ_{OWA} . The coronagraph can either channel light directly to the imager or through an IFS which disperses the light with spectral resolution R . In both cases the light is directed towards an EMCCD with effective quantum efficiency η , variation in dark current per pixel i_d , variation in readnoise per pixel per frame i_r , and variation in clock-induced charge per pixel per frame q_{cic} . Fiducial values for the two WFIRST-CGI coronagraphs and the WFIRST-CGI EMCCD

in and out of photon-counting mode are included in the Appendix in Table 1. For this work, we assume that spectra will be taken in photon-counting mode while images will not. More detail on our model’s treatment of these two modes can be found in the appendix.

We pause here to emphasize the wavelength-dependent nature of the coronagraph and detector. For a given coronagraph design Θ_{IWA} and Θ_{OWA} are fixed in units of wavelength over telescope diameter. A target system’s planet-star separation and distance from observer set its working angle. As you take images with shorter and shorter wavelengths, the coronagraph’s Θ_{OWA} may move interior to the fixed planet image, or, as you take images with longer and longer wavelengths, the coronagraph’s Θ_{IWA} may move exterior to the fixed planet image. Similarly, because C_{raw} and throughput depend on working angle in units of wavelength over telescope diameter, a target will experience different coronagraph performance as a function of wavelength (see Figure 1). Quantum efficiencies are also wavelength dependent due to the nature of the silicon and coatings used to make CCDs. Dark current, read noise, and clock-induced charge do not directly depend on wavelength, but the PSF-size and thus the number of pixels containing planet signal will scale with wavelength, incorporating more or less detector noise accordingly.

The central quantity under consideration for this model is the signal-to-noise ratio:

$$SNR \equiv \frac{Signal}{\sigma_{tot}} . \quad (6)$$

The signal is defined as:

$$Signal = r_{pl}\Delta t , \quad (7)$$

where r_{pl} is the average count rate due to photons arriving from the planet and Δt is the total exposure time spent on target. r_{pl} will depend on the brightness and distance to the star observed, the separation between planet and host star, planet size, albedo, and scattering properties, and the orbital phase angle of the planet at the time of observation. The contrast ratio for a Jupiter-Sun twin system would be 2.5×10^{-9} at quadrature assuming a Lambertian phase function. Observed from a distance of 10 pc, this gives us a rate of $\sim 2 \text{ e}^-/\text{hr}$ at 0.66 microns within a $R = 50$ spectral element (width of 0.0132 microns). The noise is defined as:

$$\sigma_{tot} = \sqrt{r_n\Delta t + \sigma_s^2} , \quad (8)$$

where r_n is the total count rate from all random noise sources, and, as in Krist et al. (2016), Lupu et al. (2016), and Nemati et al. (2017), we include an additional systematic noise term, σ_s , representing spatial confusion that arises due to speckle variation over time. This is defined as:

$$\sigma_s = f_{pp}r_{sp}\Delta t , \quad (9)$$

where f_{pp} is a number typically between 1/30 and 1/10 (Traub & Oppenheimer 2010) representing the capabilities of post-processing to remove speckles. Conservatively assuming f_{pp} of 1/10, and again a Sun-like star at a distance of 10 pc, we get an effective spatial noise term of $0.25 \text{ e}^-/\text{hr}$ at 0.66 microns within a $R = 50$ spectral element (width of 0.0132 microns). Nemati et al. (2017) emphasize that f_{pp} is, at this time, not well understood in the context of WFIRST-CGI. Proper treatment in future works must consider the dependence on working angle, exposure times, and target and calibration star magnitudes. Despite being poorly understood, it is necessary to include this term,

since speckles within the dark hole of the coronagraph can mimic planet signals in brightness and spatial extent.

The total noise count rate, r_n , is the usual summation of shot noise from target and sky backgrounds, along with detector backgrounds, combined with prefactors 1.32 and 1.20 corresponding to the assumption of background subtraction using RDI against a comparison star three magnitudes brighter than the target:

$$r_n = r_{pl} + 1.32(r_{sp} + r_z + r_{ez}) + 1.20(r_d + r_{cic} + r_r) . \quad (10)$$

Specifically, r_{pl} is the average count rate due to photons arriving from the planet, r_r is the average count rate originating from read noise, r_{sp} is the average count rate due to photons in the speckle background, r_z is the average count rate originating from zodiacal dust, r_{ez} is the average count rate originating from exozodiacal dust, r_d is the average count rate originating from dark current, and r_{cic} is the average rate of electrons originating from clock-induced charge. To understand the presence of 1.32 and 1.20 in our summation, take the example, from [Nemati et al. \(2017\)](#), of a 5th magnitude target star and a 2nd magnitude comparison star. The brightness ratio will be $10^{(5-2)/2.5}$ or 15.8, allowing us to shorten exposure times for calibration stars, thereby reducing detector related noise, and ultimately achieving a higher SNR than if we used a comparison star of equal brightness. If we spend 20% of the target time on the comparison star, the ratio of comparison star variance to target star variance will be $\frac{1}{0.2 \times 15.8}$ or 0.32. In all our calculations, we thus implicitly assume that a comparison star three magnitudes brighter than the target star was observed for 20% of the time on target. This includes the error from RDI in our SNR , while still keeping all calculations purely in terms of time on target, Δt . These calculations depend on specifics of the planet-star system being observed, so we have arbitrarily adopted a fiducial target with characteristics approximating the Sun-Jupiter system: a 4.83 V-band absolute magnitude star of type G0V, and a one Jupiter radius (R_J) planet at an orbital distance of 5 AU, all observed from a distance of 11 parsecs. In the case of direct imaging, the EMCCD will operate in analog gain mode. The stochastic nature of the amplification process results in an excess noise factor, or ENF, which multiplies contributions to r_n from planet light, speckles, zodiacal light, dark current, and clock-induced charge by an amount dependent on the actual rate of the signal. As signal increases the ENF approaches a maximum of $\sqrt{2}$ ([Denvir & Conroy 2003](#)).

Figure 22 in the Appendix illustrates the relative count rates from all contributing signal and noise sources, both for the IFS and for imaging. Figure 23 in the Appendix shows the signal-to-noise ratio achieved across the IFS coverage and in the six imaging bands for exposure times ranging from 5 to 305 hours for the IFS and from 0 to 30 hours for imaging. Looking at this figure, it is immediately clear that noise arising from the dark current dominates r_n for the IFS with the fiducial values for i_d , i_r , and q_{cic} , and typical planet-star system characteristics. Dark current is particularly detrimental to the performance of the IFS, in comparison to the imager, because the IFS incorporates ~ 4 times as many pixels in a single wavelength bin. r_n for imaging bands is mostly dominated by shot noise of the target itself and by zodiacal light.

Substituting our definitions of $Signal$ and σ_{tot} into eqn. (6) and re-arranging, we obtain the following expression for Δt as a function of SNR :

$$\Delta t = \frac{SNR^2 r_n}{r_{pl}^2 - SNR^2 f_{pp}^2 r_{sp}^2} . \quad (11)$$

Because the denominator includes a difference, if $SNR = \frac{r_{pl}}{f_{pp}r_{sp}}$ the exposure time is infinite. We thus determine that there is a maximum SNR for a given set of planet and instrument parameters which cannot be exceeded even with infinite integration time. Nemati et al. (2017) refers to this as the critical SNR :

$$SNR_{max} = \frac{r_{pl}}{f_{pp}r_{sp}}. \quad (12)$$

Figure 24 in the Appendix shows SNR_{max} as a function of wavelength for our fiducial planet-star system for three pairings of geometric albedo spectra and phase function. As demonstrated in the IFS calculations, in some cases, this critical SNR may limit our ability to accurately measure the depth of absorption features, restricting the measurement of abundances, while perhaps still allowing detection of the presence of molecular species (such as methane).

The WFIRST-CGI team is working hard to develop new techniques which may render some of these assumptions obsolete and bring about generally more favorable data quantity and quality. The most promising among these are: matched filter spectral extraction which eliminates the need for a comparison star (Kasdin et al. 2003), methods of recovering signal, even with cosmic-ray hits which could allow longer exposures, reducing clock-induced charge, raising core throughput of coronagraph designs, and improving capabilities of deformable mirrors to provide greater speckle stability. In this sense, our model may be taken as a plausible upper limit on exposure times and noise levels.

4. PLANET MODELS

4.1. *Jupiter-Neptune Hybrid Model*

In this section, we present a straightforward model for the planet-star flux ratio spectrum of a mature, wide-separation EGP. The optical geometric albedo spectrum will be determined by two simple parameters representing the atmospheric properties of the EGP, a phase curve will be adopted from empirical observations of Jupiter, and the planetary radius and orbital distance will then determine the observed planet-star flux ratio spectrum as given by eq. (1).

To model the exoplanetary geometric albedo spectrum, we postulate that the atmospheres of Jupiter and Neptune are two extremes of what the atmosphere of an unfamiliar exoplanet might resemble. With this assumption, we can construct a geometric albedo spectrum for a Jupiter-sized planet whose atmospheric properties lie between these extremes. There are a number of contrasting elements between these two giants' atmospheres that motivate this approach, including the vast difference in metallicity, with methane roughly twenty times more prevalent on Neptune than on Jupiter (Thorngrén et al. 2016), the presence of a chromophore of unknown provenance absorbing in the blue portion Jupiter's spectrum, and the significant difference in incident solar flux (Neptune is at ~ 30 AU, as compared to Jupiter's ~ 5 AU).

While both planets' reflective properties are dominated by the presence of ammonia clouds, the differences in the albedo spectra of Jupiter and Neptune are largely determined redward of $0.6 \mu\text{m}$ by the abundance of gaseous methane in the atmosphere and blueward of $0.6 \mu\text{m}$ by the presence or absence of the chromophore. Figure 3 illustrates the alternatively dominant effects of these two absorbers in the optical. Because there is no well-established correlation between methane and Jupiter's chromophore, interpolation between Jovian and Neptunian properties is here done independently for these two regions. Specifically, for a chromophore-region Jovian character P_c and methane-region Jovian character P_m (i.e. P_c or $P_m = 1$ is Jovian and P_c or $P_m = 0$ is Neptunian in the region c or

m , respectively), we interpolate the geometric albedo spectra of Jupiter and Neptune as follows:

$$A_g(\lambda) = \begin{cases} A_{g,\text{Jup}} \cdot P_c + A_{g,\text{Nep}} \cdot (1 - P_c), & \lambda < 0.55\mu\text{m} \\ A_{g,\text{Jup}} \cdot P_m + A_{g,\text{Nep}} \cdot (1 - P_m), & \lambda > 0.65\mu\text{m} \end{cases} \quad (13)$$

We arbitrarily select the region between $0.55\ \mu\text{m}$ and $0.65\ \mu\text{m}$ to transition from the blue chromophore-dominated region to the red methane-dominated region using a linearly scaling weighted average of the two formulae provided in eq. (13). Figure 4 shows the resulting albedo spectra for a variety of values of the parameters P_c and P_m .

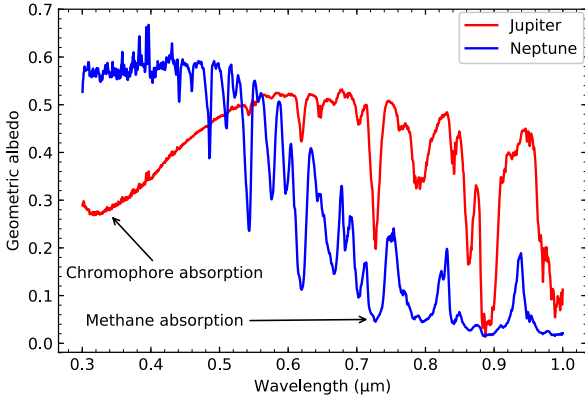


Figure 3. Comparison of the geometric albedo spectra of Jupiter and Neptune (Karkoschka 1994). The generally high albedos of both planets are dominated by the presence of ammonia clouds in the atmospheres, but the two planets maintain distinctive appearances for several reasons. The presence of a chromophore on Jupiter absorbing in the blue is largely responsible for its red color; the order of magnitude higher abundance of methane on Neptune results in even greater absorptions in the red and gives Neptune its blue tint. The sharp dips in albedo at $0.62\ \mu\text{m}$, $0.72\ \mu\text{m}$, $0.79\ \mu\text{m}$, $0.86\ \mu\text{m}$, $0.89\ \mu\text{m}$, and $0.99\ \mu\text{m}$ for both Jupiter and Neptune are characteristic of methane, but its higher abundance on Neptune results in generally lower geometric albedos redward of roughly $0.6\ \mu\text{m}$.

By separating the Jovian character of the red and blue regions of the spectrum, we allow P_c and P_m to function loosely as metrics of the chromophore and methane content of an atmosphere. In the event that WFIRST-CGI only characterizes a few planets, this model could distinguish a Jupiter-like planet from a Neptune-like planet. If a larger number of targets are characterized, fits to this model can provide information about trends in methane and chromophore abundances across planets of varying mass and orbital distance, as well as across planets orbiting a variety of stellar types. These trends may then be interpreted to shed some light on the nature and origin of Jupiter's chromophore and the determinants of metal abundances in planetary atmospheres.

Once the geometric albedo spectrum has been established for some hybrid of Jupiter and Neptune, the planet-star flux ratio spectrum for an EGP of known radius and Keplerian elements can be determined by applying the classical phase function (see eq. 1 and §2.2). Ideally we would have an empirical phase curve for Jupiter and Neptune with a wavelength dependence resolved on the order with which the WFIRST-CGI IFS observations will be done. However, observational data on the

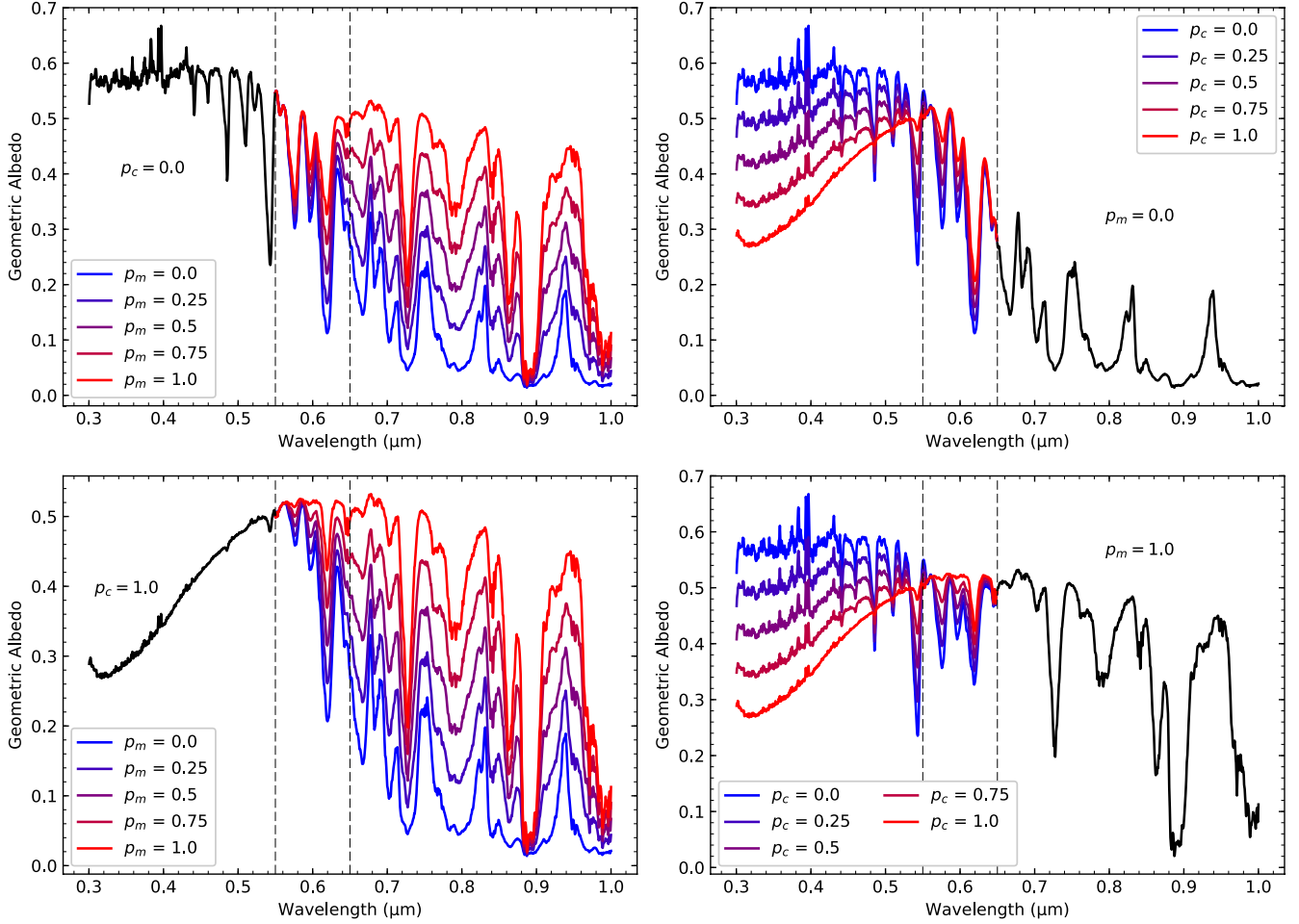


Figure 4. Piece-wise interpolations of the geometric albedo spectra of Jupiter and Neptune with a transition region between $0.55 \mu\text{m}$ and $0.65 \mu\text{m}$. **Left:** Redward of $0.65 \mu\text{m}$, the spectrum is fully Neptunian (top) or Jovian (bottom), while the chromophore-dominated region is varied between Jovian ($P_c = 1.0$) and Neptunian ($P_c = 0.0$) conditions. **Right:** Blueward of $0.55 \mu\text{m}$, the spectrum is fully Neptunian (top) or Jovian (bottom), while the methane-dominated region is varied between Jovian ($P_m = 1.0$) and Neptunian ($P_m = 0.0$) conditions. The left column shows that redward of $\sim 0.6 \mu\text{m}$, the abundance of methane largely determines the geometric albedo of the planet; the closer the hybrid is to having a Neptunian atmosphere ($P_m = 0.0$), the lower its albedo spectrum is (note particularly the sharp dips at $0.62 \mu\text{m}$, $0.72 \mu\text{m}$, $0.79 \mu\text{m}$, $0.86 \mu\text{m}$, $0.89 \mu\text{m}$, and $0.99 \mu\text{m}$ associated with methane absorption). The right column shows that blueward of $\sim 0.6 \mu\text{m}$, the albedo is instead determined by the absorption of a chromophore whose abundance is maximized for hybrid planets with Jovian character ($P_c = 1.0$).

phase curves of Jupiter and Neptune are limited. Early reports provided only one phase curve to roughly represent the behaviors of Jupiter, Saturn, Uranus, and Neptune (Pace 1971). More recent measurements from Cassini provide phase curves of Jupiter between $\alpha = 0^\circ$ and $\alpha \approx 140^\circ$ in three optical bandpasses. These data are extrapolated to all phase angles by Mayorga et al. (2016), but they still fail to account for the variation of phase curves over small wavelength intervals. Theoretical models for exoplanetary phase curves (Dyudina et al. 2005, 2016; Cahoy et al. 2010; Hu et al. 2015)

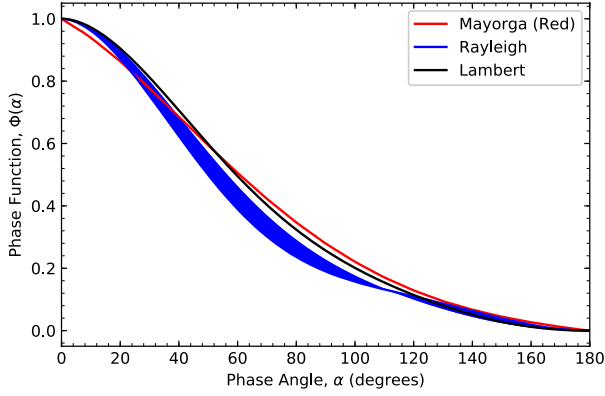


Figure 5. Empirical phase curve of Jupiter collected through Cassini’s red filter (red curve, [Mayorga et al. 2016](#)), compared with the Lambertian phase curve (black) and a suite of wavelength-dependent phase curves for a uniform atmosphere with purely Rayleigh scattering (blue). Note that empirical phase curves through other filters do not vary significantly from the one presented here. The suite of Rayleigh scattering curves was generated analytically using the formalism of [Madhusudhan & Burrows \(2012\)](#); for any given wavelength, the resulting phase curve will be contained within the bounded blue region. The bounds correspond to the phase curves associated with the lowest and highest geometric albedos in Jupiter’s spectrum, which are roughly consistent with the extreme albedos of all hybrid spectra.

limit their scope to exclude Neptune-like planets and also lack a precise wavelength dependence. Of these limited options, we select, for the hybrid model, the red-bandpass empirical Jovian phase curve from the most recent observations ([Mayorga et al. 2016](#)) to represent the true phase curve of our fiducial EGP at all wavelengths. In §5, we compare our results derived under this empirical phase curve to those that would be produced under a Lambertian phase curve. The Lambertian assumption has been specifically shown to overestimate reflectivities at most phase angles ([Greco & Burrows 2015](#); [Mayorga et al. 2016](#)). Nevertheless, the prominence of Lambertian phase curves in recent literature motivate this comparison.

In this paper, we also seek to understand the degree to which uncertainties in the wavelength dependence of EGP phase curves will affect characterization of their atmospheres (see §5). This requires a wavelength-dependent phase curve to pair with our geometric albedo models. Since wavelength-dependent empirical phase curves are not yet available, we implement a phase curve representative of a uniform atmosphere dominated by Rayleigh scattering². To produce the phase curves corresponding to Rayleigh-scattering atmospheres, we employ the methodology³ presented by [Madhusudhan & Burrows \(2012\)](#) to generate a phase curve for an EGP with any given albedo spectrum at any given wavelength. By itself, this formalism produces a geometric albedo and phase curve for an atmosphere dominated by Rayleigh scattering under the assumption of a constant single-scattering albedo representative of a uniform atmosphere. Under this formalism, varying the scattering albedo—the ratio of scattering cross section to the summed scattering and absorption cross sections—will necessarily and monotonically vary the resulting geometric albedo and phase curve. We utilize the one-to-one mapping between scattering and geometric albedos to invert a known geometric albedo spectrum into a scat-

² For all calculations involving Rayleigh scattering, the vector formalism was used.

³ See Section 2.4 in [Madhusudhan & Burrows \(2012\)](#) for an explanation of the formalisms and calculations involved.

tering albedo spectrum, which can then be mapped analytically to a suite of wavelength-dependent phase curves with the same resolution as the input geometric albedo spectrum. Realistically, the assumptions of uniform scattering type and the resulting ability to map a geometric albedo to a unique phase curve might not hold true, but the phase curves resulting from this methodology approximate Jupiter’s empirical phase curve fairly well. Figure 5 compares the range of phase curves produced thusly with a Lambertian phase curve and Jupiter’s phase curve from [Mayorga et al. \(2016\)](#).

The methodology presented in §2.2 can be used in tandem with the albedo and phase curve models of this section to generate light curves through WFIRST filters for an arbitrary EGP. To do this, we generate an entire spectrum of planet-star flux ratios at each time t , combine that with the stellar spectrum to produce a spectrum of exoplanetary flux, and take the ratio of filter-integrated planet flux to filter-integrated star flux:

$$\frac{F_p(t)}{F_\star} = \frac{\int_{-\infty}^{\infty} F_p(t, \lambda) \cdot T(\lambda) d\lambda}{\int_{-\infty}^{\infty} F_\star(\lambda) \cdot T(\lambda) d\lambda}, \quad (14)$$

where t , as previously, represents the time elapsed since periastron and the filter transmission $T(\lambda)$ defines the bandpass through which the light curve is generated. Figure 6 compares the resulting light curves for Jovian, Neptune-like, and hybrid planets in various orbits through each of the filters to be incorporated on WFIRST, where we have assumed flat transmission functions around their appropriate central wavelengths.

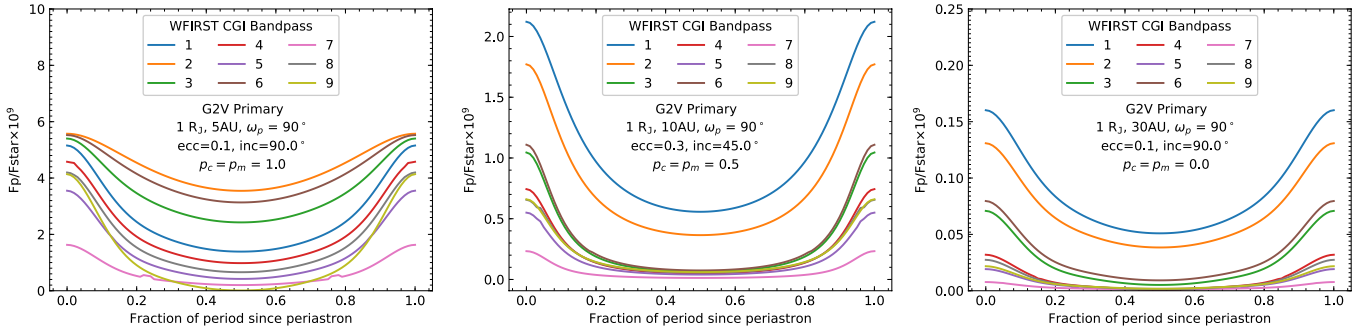


Figure 6. Light curves for an assortment of hypothetical EGP’s as they would appear through WFIRST filters. The **left** panel shows the light curves generated from a fully Jovian planet in a low-eccentricity, edge-on orbit 5 AU from its parent star. The **right** panel simulates a Neptunian (but still Jupiter-sized) EGP in a similar orbit 30 AU from the parent star. The **center** panel displays the light curves for a 50% hybrid planet in a more eccentric orbit, now inclined at 45° , 10 AU from the parent star. In all calculations, the argument of periastron ω_p is assumed to be 90° , and the primary star is assumed to be Sun-like (G2 V). Note that the light curve through CGI Bandpass 7 (at roughly $0.89 \mu\text{m}$) depicts significantly lower planet-star flux ratios for all modeled systems at all times; this corresponds to the significant methane absorption within the band. In all three cases, variation in the color of the planet with orbital phase is apparent.

4.2. *CoolTLUSTY: Varying Metallicity*

In addition to the Jupiter/Neptune hybrid model, we also generated reflection spectra and albedos using the atmosphere and spectral code *CoolTLUSTY* ([Hubeny & Lanz 1995](#); [Burrows et al. 2004](#); [Sudarsky et al. 2005](#)). This code solves self-consistent atmospheres under stellar irradiation, using a

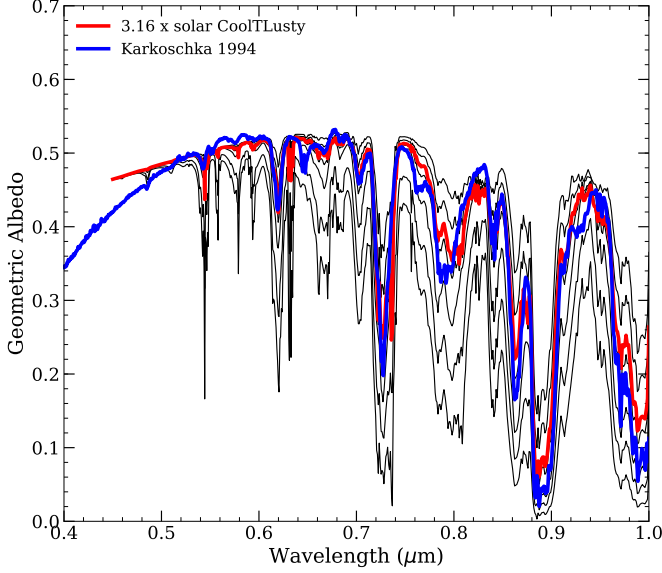


Figure 7. Example geometric albedo spectra generated using *CoolTLusty* to first match the measured Jovian spectrum (Karkoschka 1994, bold blue line) at a fixed metallicity of 0.5 dex, $\sim 3.16 \times$ solar elemental abundances, (bold red line), and then fixing all cloud, haze, and particle parameters and simply perturbing metallicity between 1.0 and 30 times solar metallicity (thin black lines). The match between Jupiter’s observed spectra and the best fit with *CoolTLusty* is not perfect, but it is certainly adequate for the purposes of this study.

detailed suite of thermochemical and opacity data (Burrows & Sharp 1999, augmented to incorporate the ExoMol methane opacities of Yurchenko & Tennyson 2014). However, for albedo calculations for planets with cool atmospheres, once the assumption of chemical equilibrium is made and the atmospheric temperatures are below ~ 300 Kelvin, variations in the atmospheric temperatures with altitude do not translate into significant compositional or opacity variations. The atmospheres for such giant exoplanets will be dominated by molecular hydrogen and helium (presumably in solar ratios) and gaseous methane. As seen in the atmospheres of Jupiter and Saturn, ammonia is likely to be mostly in condensed phase and constitute the bulk of the scattering clouds. Some water in vapor and cloud form could also be present, as could other condensates (such as the chromophores seen in the atmospheres of Jupiter and Saturn) or tholins, such as are inferred in Titan’s atmosphere. Whatever the condensates (clouds and hazes), they are not at present well-modeled by exoplanet theorists. We don’t really know what the species are, nor their spatial (vertical and horizontal) variations, nor their particle sizes and shapes. Given this uncertainty, for the purposes of this class of models we merely keep the temperatures below ~ 200 K, assume a uniform scattering cloud and a uniform distribution of an absorber. The scattering cloud in our *CoolTLusty* model has a scattering opacity set above a wavelength $0.84 \mu\text{m}$ at a constant $0.002 \text{ cm}^2 \text{ g}^{-1}$ and below a wavelength of $0.84 \mu\text{m}$ it assumes a $\frac{1}{\lambda^{2.5}}$ behavior. The uniform haze absorber is taken to be Titan tholins (Khare et al. 1984) with an assumed atomic weight of 100, a model particle size of $0.05 \mu\text{m}$, and a number fraction of 3.3×10^{-10} . Even with such a low abundance, the tholin haze can markedly affect the albedo at short wavelengths and serves as our chromophore. These specific numbers and constituents were chosen to fit Jupiter’s albedo spectrum (Karkoschka 1994, 1998) for an atmosphere with a metallicity of 0.5 dex, $\sim 3.16 \times$ solar elemental abundances, insolated with a blackbody solar spectrum at 5777 K. As Figure

7 demonstrates, the fit to Jupiter’s albedo spectrum is rather good, though not perfect. With this background model, we then varied only the metallicity to include solar, $10\times$ solar, and $30\times$ solar. In this way, we have generated a simple model suite that crudely captures the possible metallicity (read methane) dependence of such exoplanet albedos. These other models are also provided on Figure 7. We again pair these models for geometric albedo spectra with the empirical Jovian phase curve of Mayorga et al. (2016) and a Lambertian phase curve to compute planet-star flux ratios.

The *CoolTLusty* approach captures differences across the WFIRST-CGI spectral coverage in one physically-motivated parameter, making it a useful tool for interpreting WFIRST-CGI data and other similar observations. Nevertheless, this approach has some drawbacks: the assumption of known cloud and haze scattering properties could introduce a systematic bias in metallicities fit to EGP’s if they deviate significantly from what is expected, and the set of models accounting for solar to $30\times$ solar metallicities does not span as wide a range of geometric albedo spectral shapes as the previously presented Neptune-Jupiter hybrid model (compare Figure 4 and 7).

5. RESULTS

WFIRST-CGI has the potential to observe planet-star systems with a wide array of characteristics. As the signal and instrument models presented in §4 and §3 illustrate, many factors will determine the relative contributions of signal and noise over exposure time: distance from observer, spectral type and magnitude of host star, planet-star separation, planet radius, the planet’s wavelength-dependent geometric albedo, the orbital phase at the time of observation, the wavelength-dependent performance of the coronagraph, and the observing strategy adopted by the WFIRST-CGI mission.

In order to present a realistic and coherent understanding of WFIRST-CGI’s science potential in the context of our two planet geometric albedo models, we adopt the following planet-star characteristics as our fiducial target: a \sim Sun-like star with spectral type G0V and an absolute V-band magnitude of 4.83 residing 11 pc from Earth, a $1.0 R_J$ planet, a planet-star separation of 5 AU, and a circular orbit seen edge-on, and observed at orbital phase $\alpha=60^\circ$. These characteristics are chosen to be similar to the Jupiter-Sun system, and because they keep the target within the functional working angle of both coronagraphs across the full range of spectral coverage, while maintaining consistency with the physical characteristics of detected RV planets deemed suitable targets for WFIRST-CGI (see section 5.5).

First, we use this fiducial system to illustrate exposure time and signal-to-noise ratio relations in all three IFS bands and in all six imaging bands. Then, we explore the degree to which three observational scenarios utilizing various combinations of imaging and IFS coverage can constrain our two simple planet geometric albedo models and planet radius. Finally, we set aside this fiducial system and compute achievable signal-to-noise ratios for known RV planets, selecting two promising target systems (47 UMa c and Upsilon And d) and simulating observations for the same three scenarios.

5.1. Signal-to-noise Ratios and Exposure Times

Relating SNR to exposure time is an essential part of planning observational strategies with WFIRST-CGI. We explored how this relation varies with radius of the target planet, planet-star separation, degree of methane absorption, and orbital phase by computing values of SNR for the central spectral element of each IFS wavelength bin (see Figure 8 and Figure 9), and for the six imaging bandpasses (see Figure 10 and Figure 11), all as a function of on-target exposure time. These figures provide a clear picture of the general scaling of SNR with time for the model presented in

§3. For low exposure times, SNR increases with the square root of exposure time, exhibiting a slope of 0.5 on our log-log plots. At longer exposure times, SNR asymptotically approaches the maximum value given by eq. (12). Integration times above 300 hours are not feasible for the IFS and integration times above 48 hours are not feasible for imaging bands; therefore, these regions in the figures are shaded gray. Previous works identified an SNR of five as sufficient to gain useful science information with spectra (Lupu et al. 2016), so the region below this threshold is shaded purple. In the case of our fiducial system and variations on it, the SNR attained is limited by the 300-hour maximum exposure time for the IFS and the 48-hour maximum exposure time for the imagers, rather than the maximum SNR (see how the curves flatten in the gray shaded regions of Figs. 8 and 9). The same is true of other known RV targets shown in Figs. 21 and 20.

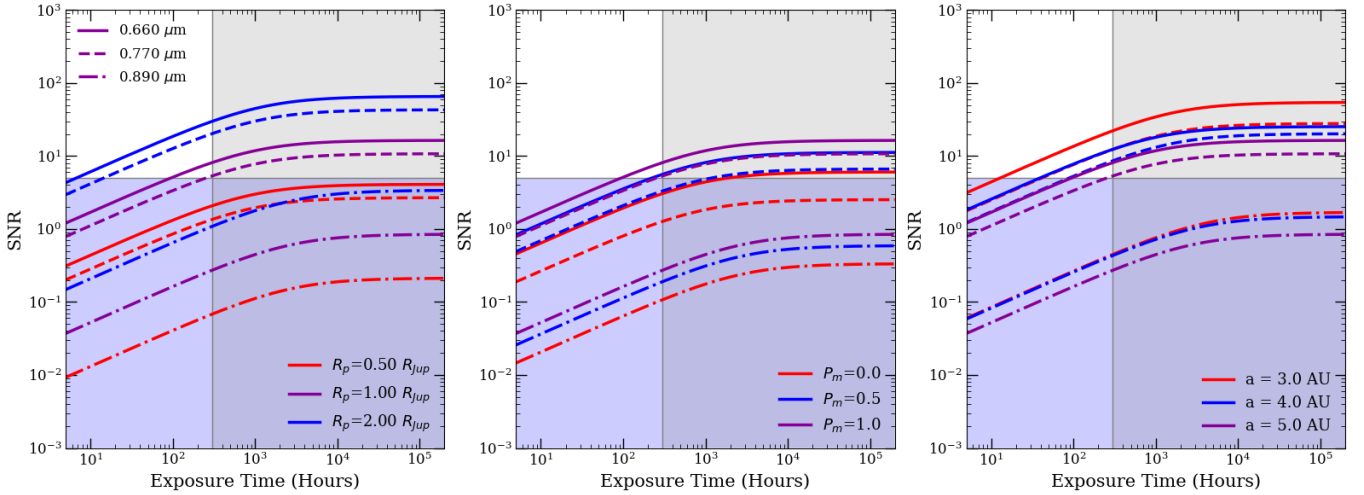


Figure 8. SNR as function of exposure time for the $R = 50$ spectral element of the IFS at the three band centers. In all three panels, solid lines correspond to $0.66 \mu\text{m}$, dashed lines correspond to $0.77 \mu\text{m}$, and dash-dotted lines correspond to $0.89 \mu\text{m}$. Colors indicate a variation in a single parameter from the fiducial star planet system: a Jupiter-size planet, with a Jovian geometric albedo spectrum, with separation of 5 AU, orbiting a Sun-like star, observed from 11 parsecs away at $\alpha=60^\circ$ assuming the observed phase curve of Jupiter (Mayorga et al. 2016). The **left** panel varies planet radius. The **center** panel varies the value of the methane-like absorption parameter P_m for the Jupiter-Neptune Hybrid model. The **right** panel varies the semi-major axis of the planet's orbit, which is also the separation because we have assumed circular orbits. Exposure times above 300 hours are shaded gray because they exceed the maximum feasible exposure time for WFIRST-CGI. SNR values below 5 are shaded purple because this is a threshold above which previous work has concluded that the spectra are scientifically useful. If we ignore the σ_s correction term in eq. 6, SNR scales roughly with the square root of the exposure time. This shape is apparent in all panels in the $\sim 1/2$ slope on the log-log scale. At late times, the SNR asymptotes to the maximum achievable value, seen as the curve flattens off. The SNR 's achieved for $0.89 \mu\text{m}$ hardly exceed 1 since it falls near the bottom of a strong methane absorption feature and in the region where quantum efficiency has plunged. Increasing planet radius increases SNR across all regions of the spectrum in a similar manner. Lower values of P_m indicate a planet closer to Neptune-level methane absorption and its correspondingly very low albedos, while higher values of P_m indicate a planet closer to Jupiter's methane absorption with slightly higher albedos. Changing the semi-major axis changes both the amount of stellar insolation reaching the planet, and the working angle of the planet on the detector.

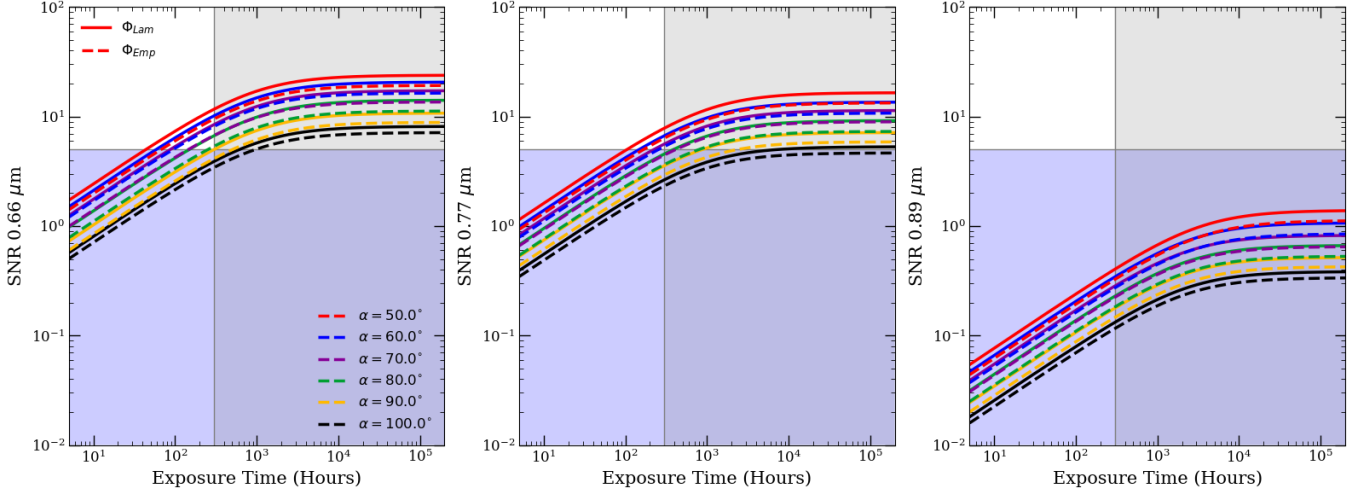


Figure 9. *SNR* as a function of exposure time for the $R = 50$ spectral element of the IFS at the three band centers ($0.66\mu\text{m}$ on the **left**, $0.77\mu\text{m}$ in the **center**, and $0.89\mu\text{m}$ on the **right**). Colors indicate the orbital phase for which the *SNR* is calculated, with all other planet-star system characteristics held to our fiducial values: a sun-like star observed from a distance of 11 pc, orbited by a Jupiter-like planet at a separation of 5 AU with an edge-on orbit. In all panels, solid lines correspond to the Lambertian phase function and dashed lines correspond to the empirical Jovian phase function of Mayorga et al. 2016. Gray shading indicates exposure times above 300 hours which will not be feasible with WFIRST-CGI. Purple shading indicates $SNR < 5$. It is clear that, as expected, the Lambertian phase curves estimate a higher *SNR* for any given exposure time than the observed Jovian phase curve. See Figure 5 for a comparison of the Lambertian and empirical phase curves. It is also apparent that, for our fiducial system, phase angles between 50° and 90° produce $SNR > 5$ within 300 hours, while larger phase angles do not.

WFIRST-CGI is just barely able to attain an *SNR* above five for our approximate Jupiter-Sun system with the IFS (see purple lines in Figure 8), but the variations of planet radius, planet-star separation, and orbital phase angle demonstrate that many realistic target systems will provide similar or superior data quality relative to our fiducial system in the same exposure times. Exposure times for the IFS to attain spectra with $SNR \sim 5$ for our fiducial system will be on the order of hundreds of hours, with exact times depending on the planet-star system characteristics. Imaging in the $0.575\text{-}\mu\text{m}$ and $0.661\text{-}\mu\text{m}$ bands will easily attain *SNR*'s of 25 within the maximum imaging time for our fiducial system. The $0.721\text{-}\mu\text{m}$ band will attain an *SNR* of 10, while the longer wavelength $0.883\text{-}\mu\text{m}$ and $0.940\text{-}\mu\text{m}$ bands will just barely reach an *SNR* of 4 to 5 within 48 hours. The $0.506\text{-}\mu\text{m}$ band reaches an *SNR* around 8, rather than the expected *SNR* of 25 to 30, due to the degradation in coronagraph contrast near the outer working angle. Many planet systems will have working angles such that the $0.506\text{-}\mu\text{m}$ band falls within the coronagraph's region of peak performance, and thus achieve higher *SNR*'s. The near order-of-magnitude variation in *SNR* for a fixed exposure time between the six imaging bands arises from their varying widths, the wavelength dependence of the noise and quantum efficiency, and the varying geometric albedo of the target planet.

When all other characteristics are held to our fiducial values, exposure times of 100 hours achieve an *SNR* of ~ 5 for a Jupiter-sized planet, ~ 15 for a planet with twice Jupiter's radius, and only ~ 2 for a planet with half of Jupiter's radius at the centers of the $0.66\text{-}\mu\text{m}$ and $0.77\text{-}\mu\text{m}$ IFS bands. The *SNR* is less than 5 for all three planet radii at the center of the $0.89\text{-}\mu\text{m}$ IFS band. Increasing planet radius to

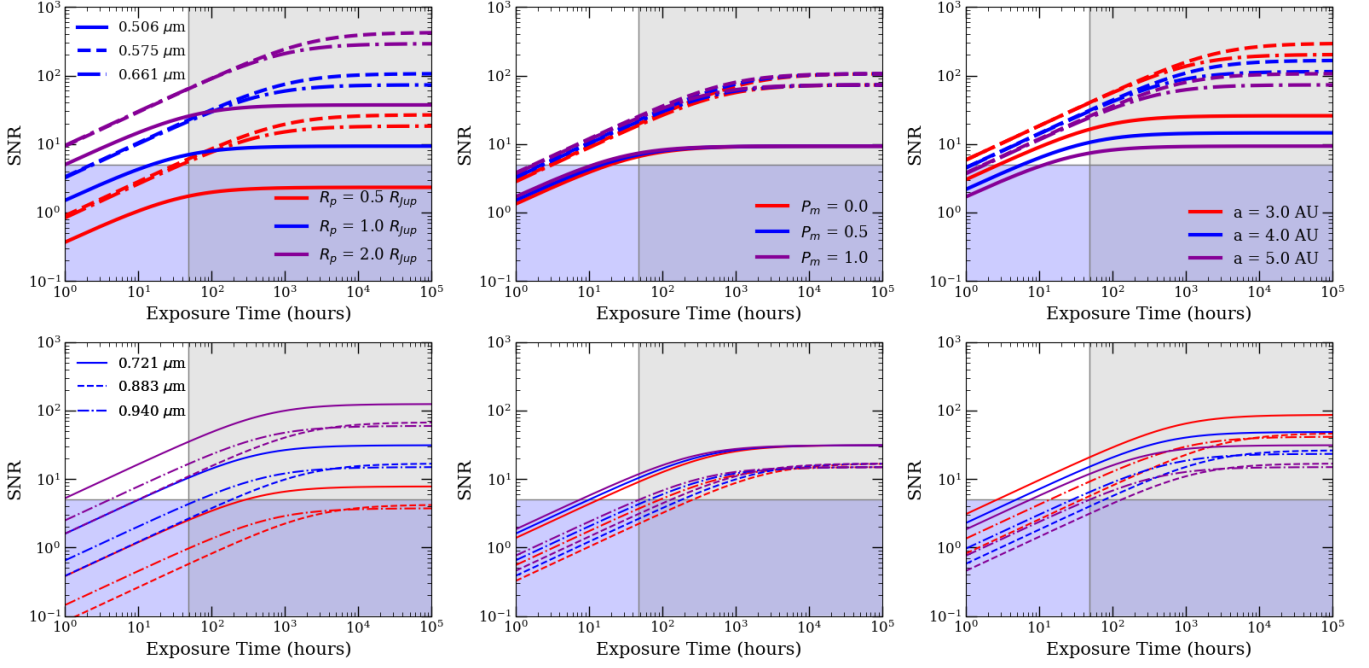


Figure 10. *SNR* as a function of exposure time for the six imaging bandpasses. The **top** row shows the 0.506- μm , 0.575- μm , and 0.661- μm bands as solid, dashed and dash-dotted lines respectively. The **bottom** row shows the 0.721- μm , 0.883- μm , and 0.940- μm bands, as thinner solid, dashed, and dash-dotted lines respectively. Colors indicate a variation in radius (left column), long-wavelength absorption (center column), and semi-major axis (right column), with all other planet-star system characteristics held to our fiducial values: a sun-like star observed from a distance of 11 pc, orbited by a Jupiter-like planet at a separation of 5 AU with an edge-on orbit, observed when planet is at an orbital phase angle of 60° . Gray shading indicates exposure times above 48 hours. Purple shading indicates *SNR* below five. Similar to the IFS, the imaging *SNR* scales with the square root of the exposure time at short times, eventually asymptoting to a maximum value at longer times. Dependence on planet radius and planet-star separation are similar to the IFS, but the dependence on methane-like absorption is notably less significant. This is due to the width of the imaging bands compared to a single spectral element of the IFS. Aside from the 0.94- μm band which only attains reasonable *SNR* within 48 hours for the 2 R_J radius planet at a separation of 5 pc, or for the 1 R_J radius planet at a separation of 3 AU, the imaging bands all attain desirable *SNR* levels across a variety of realistic planet radii, methane absorption levels, and planet-star separations.

2.0 R_J allows observations to reach an *SNR* greater than 5 in all six imaging bands within 48 hours for each band, with some bands capable of reaching a much higher *SNR* (up to 70). Again assuming our fiducial system, at the center of the 0.66- μm IFS filter, planet's with Neptune-like methane absorption features attain an *SNR* of only ~ 2.5 at 300 hours (the maximum feasible exposure time), compared to an *SNR* of ~ 10 for a planet with Jupiter-like methane absorption. Varying methane absorption levels has a minimal effect on imaging count rates compared to the effect on the IFS spectral elements. The wider bands include enough continuum that they still receive reasonable numbers of photons even with Neptune-level methane absorption. Moving the planet in from our fiducial planet-star separation of 5 AU to 3 AU improves the *SNR* by about a factor of two for both the imaging bands and the IFS. These results make it clear that the longest wavelength band for the IFS will only yield useful *SNR* data under the most favorable planet-star system circumstances, and even the

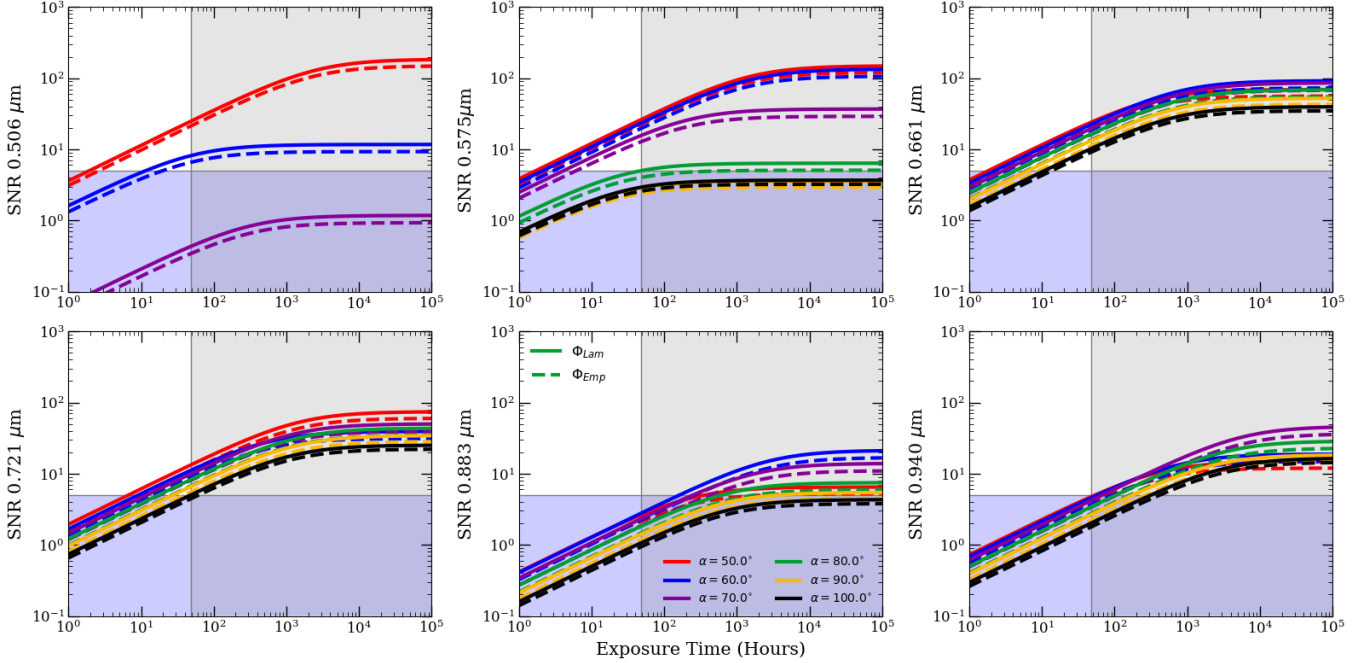


Figure 11. *SNR* as a function of exposure time for the six WFIRST-CGI imaging bands (each wavelength shown in a separate panel and labeled) computed at orbital phase angles from 50-100° as indicated by the line colors. Dashed lines are the empirical Jovian phase function from [Mayorga et al. 2016](#), compared to a classical Lambertian phase function indicated by a solid line. The gray shaded region again indicates exposure times above 48 hours and the purple shading indicates *SNR* below five. Differences are much more pronounced for the 0.506- μm band and the 0.575- μm band. These shorter wavelengths fall near the outer working angle of the coronagraph (see Figure 1), so they see significantly different coronagraph performance as their phase angle changes. For the 0.506- μm band, the phase angles in the range 80° to 100° fall exterior to the the outer working angle of the coronagraph. So long as phase angle does not draw the planet outside the peak performing working angles of the coronagraph, imaging *SNR* is adequate across this range of phase angles. Similar to Figure 9, the Lambertian phase function predicts a higher *SNR* than the empirical phase function for a given exposure time.

longest wavelength imaging bands perform significantly worse than the shorter wavelength bands. Regardless of planet characteristics, at the longer wavelengths where typical gas giants have lower albedos, quantum efficiencies are lower, and PSF sizes are larger, the *SNR* is significantly lower than at the shorter wavelengths. Attaining an *SNR* of five at the bottom of individual absorption features, especially the 0.89- μm line, will likely not be possible for any known RV targets as WFIRST-CGI IFS is currently configured. Unknown planets around nearer stars could change this, but it may be more sensible to eliminate the longest wavelength IFS filter centered at 0.89 μm , allowing valuable observing time to be allotted elsewhere. These wavelengths can be better probed by narrow-band imaging.

Considering Figure 9 and Figure 11, it is apparent that observations should be done while planets are at orbital phase angles between 50° and 70°. Assuming a Lambertian phase function results in a higher *SNR* than the observed phase function of Jupiter for any given exposure time, with the largest difference in the range $\alpha=50^\circ$ to $\alpha=90^\circ$, the most likely phases WFIRST-CGI will target. This is consistent with the long noted discrepancy shown in Figure 5, and emphasizes the importance of

factoring uncertainties in planet phase and phase function into future analyses. At $\alpha > 110^\circ$ and $\alpha < 20^\circ$, differences between the two phase functions are less pronounced.

We also computed the exposure time necessary to reach an SNR of five across the full IFS wavelength coverage, as a function of wavelength and phase, wavelength and exozodi level, wavelength and planet radius, and wavelength and planet-star separation (see Figure 12). Integration times were again computed assuming our fiducial planet-star system, aside from the parameter which was being varied. These calculations of exposure time in terms of two parameters make it apparent that only certain portions of the exoplanetary spectrum might attain adequate SNR or even be observable at all depending upon the planet-star system characteristics. Any region in Figure 12 that is green, blue, purple, or black is unable to reach an SNR of 5 for our fiducial system with WFIRST-CGI’s IFS, either due to SNR_{max} limitations or due to exposure times exceeding the mission capabilities and resources. These regions occur in deep absorption features in both the stellar spectrum and the planet albedo spectrum, below a minimum radius of $\sim 0.8 R_J$, and above a maximum orbital phase of $\alpha \sim 90^\circ$. White portions of the figures represent areas where the planet will fall outside the inner or outer working angles of the coronagraph (see Figure 1).

It is not surprising that planet radius, planet-star separation, and orbital phase angle all strongly influence integration times to reach an SNR of five. In our model, exposure time scales approximately linearly with planet signal, if we ignore the σ_s correction term (combining eq. 6 and 8). This is because the SNR scales approximately with the square root of the planet count rate, and the exposure time in turn goes as the square of the SNR . Planet photon count rates scale with radius squared (see eq. 1), so exposure times will scale with radius squared. Similarly, planet count rates scale inversely with the square of planet-star separation, but we must also fold in the effects of varying the working angle of the coronagraph for a fixed observing distance. Varying the phase angle affects the count rates from the planet according to the phase function, and again, by changing the working angle where the planet falls on the coronagraph, it will move through different levels of coronagraph performance. In contrast, exozodi levels do not have a strong effect at all. N_{ez} multiplies directly into exozodi count rates, but exozodi is not a dominant noise term for the IFS, particularly at a separation of 5 AU and for a $1.0 R_J$ planet (see Figure 22). Therefore we see in the upper right panel that it causes little variation in the requisite exposure times for any given wavelength. This is consistent with the findings of Robinson et al. (2016).

5.1.1. *The Smallest Planets Observable with WFIRST-CGI*

Just how small of a target planet can be seen with WFIRST-CGI? As §5.1 explains, the ratio of signal and noise from a given star-planet system depends on many factors. Planets that are observable near full illumination and are closer to their host stars (all while maintaining the high albedos associated with clouds) will be brightest for any given radius. The limiting radius is thus highly dependent on the distance to the target system for three reasons: (1) nearer stars will allow observations of planets with smaller separations, (2) observations can be done closer to full phase, and (3) more photons reach the observer, scaling with the inverse square of distance. We computed integration times to reach an SNR of five for a planet with a radius of $0.4 R_J$ and a Jovian geometric albedo spectrum, as a function of wavelength and separation, and wavelength and orbital phase, at various observer distances (similar to Figure 12). These calculations indicate that WFIRST-CGI may obtain spectra for a Neptune-sized planet 7 parsecs from Earth if it is at a separation of 2 AU and observed at orbital phase angles between 35° and 80° . If the planet-star system is instead 9 parsecs

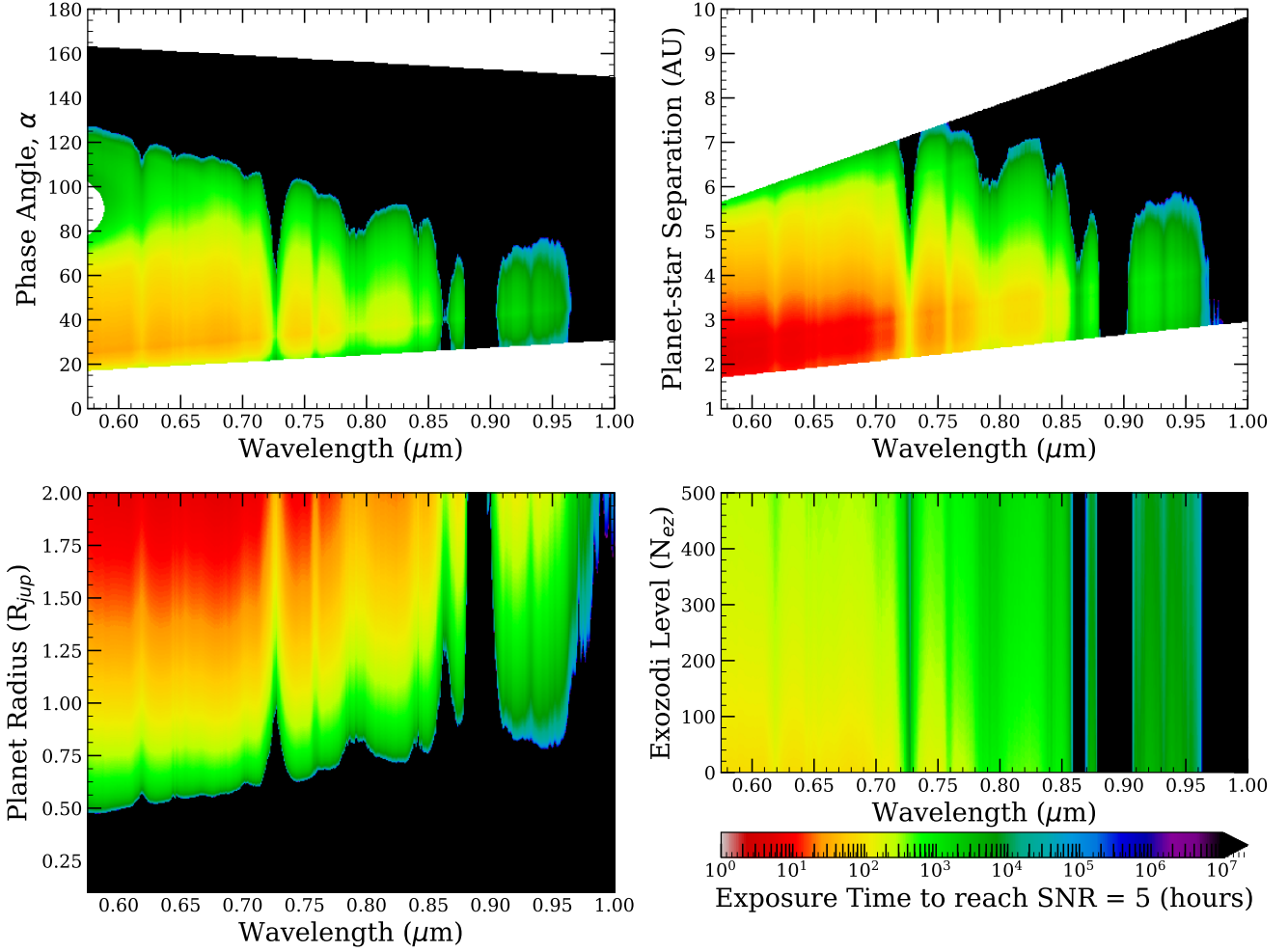


Figure 12. Integration time required to reach an SNR of 5 in each spectral element of the IFS as a function of phase angle, exo-zodi level, planet radius, and planet-star separation vs. wavelength. Integration times were computed assuming our fiducial planet-star system aside from the parameter which was being varied: 4.83 V-magnitude G0V type host star with a $1.0 R_J$ planet orbiting at a separation of 5 AU, all observed from a distance of 11 pc. We assume a Jovian geometric albedo spectra and [Mayorga et al. 2016](#)’s empirical Jovian phase curve at $\alpha=60^\circ$. Integration times above 300 hours are not feasible, so any region that is green, blue, purple or black can be interpreted as unable to reach an SNR of 5 with WFIRST-CGI. Note that some subsection of the black regions have $SNR_{crit} < 5$, indicating an infinite integration time on this plot. The white space in the upper left and upper right panels represent areas where the planet will fall outside the inner or outer working angle of the coronagraph at that wavelength. These results indicate that for systems like our fiducial system (that is, systems at a distance of 11 pc), observations should be done when planets are at phase angles between 20° to 80° , exozodi does not have a large effect on exposure times to reach SNR of 5, planets smaller than Neptune will not be observable, and separations of 2.5 to 4 AU provide the best balance of long-wavelength coverage and planet signal.

from Earth and the orbital distance is still 2 AU, it will not attain useful SNR ’s with the IFS, though it could be detected by shorter wavelength imaging. Between 7 and 9 pc, IFS observations may be successful depending on the geometric albedo of the planet. Moving the planet to a wider separation quickly lowers the SNR and lengthens exposure times. As currently planned, observing planets with

radii significantly smaller than Neptune would be plausible for very nearby stars with the imager only. Lowering the resolution of the spectrograph could allow observations of smaller planets with the IFS. Overall, we find that WFIRST-CGI will have the most success observing roughly Jupiter-sized planets, but it may still be able to probe smaller Neptune-sized planets under the right circumstances.

5.2. *Simulating Observations and Fitting Procedure*

Given our planet models and Nemati et al. (2017)’s model for the WFIRST-CGI signal-to-noise ratio, it is straightforward to generate a noisy spectrum or photometric measurement given an on-target exposure time. To generate a single realization of a noisy synthetic observation, for each photometric and spectral bin we could draw a random value from a normal distribution with the mean being the true value of the spectrum/photometry and the variance being σ_{tot} , as defined in eq. (8). We choose instead, however, to use the true clean signal values and assign them the uncertainties σ_{tot} in order to directly capture the nature of the distribution. We consider three possible observing cases:

Case One: Full IFS coverage across the three $\sim 18\%$ width bands at $0.66\ \mu\text{m}$, $0.77\ \mu\text{m}$, and $0.89\ \mu\text{m}$ and the two shortest wavelength imaging filters centered at $0.506\ \mu\text{m}$ and $0.575\ \mu\text{m}$.

Case Two: Imaging only, done in all six bands: $0.506\ \mu\text{m}$, $0.575\ \mu\text{m}$, $0.661\ \mu\text{m}$, $0.721\ \mu\text{m}$, $0.884\ \mu\text{m}$, and $0.940\ \mu\text{m}$.

Case Three: One $\sim 18\%$ width IFS band centered at $0.7\ \mu\text{m}$ and one imaging band at $0.575\ \mu\text{m}$.

In case one, we compute the signal and noise contributions given an exposure time for each wavelength bin spanning the three IFS filters with a spectral resolution $R = 50$. Note that this results in slightly better coverage where the filters overlap, and that the total exposure time for the observing case will be three times the nominal on-target time since one must sum the times for all three IFS filters. We also compute the signal and noise contributions in the imaging filters centered at $0.506\ \mu\text{m}$ and $0.575\ \mu\text{m}$ with an SNR of 30 independent of the exposure time adopted for the IFS, since the imaging will contribute a relatively small fraction of the total observing time. In case two, we compute the signal and noise contributions given an exposure time for each imaging bandpass. For the sake of simplicity, we use the same exposure time for each bandpass, resulting in variable SNR for the different photometric measurements and a total time for the observing case of six times the reported on-target exposure time. In practice, exposure times would likely be varied to avoid unnecessarily high SNR in the brighter filters. In case three, we compute signal and noise contributions given an exposure time for each wavelength bin spanning a single IFS filter with a spectral resolution $R = 50$, and include an imaging band at $0.575\ \mu\text{m}$. This will clearly provide less information due to the more limited wavelength coverage, but the total exposure time for the observing case will be about a third of observing case one.

To investigate the synthetic observations’ ability to constrain the planet geometric albedo model parameters and the radius of the planet, we carry out a simultaneous fit of all parameters using *emcee* (Foreman-Mackey et al. 2013), a parallelized python implementation of the affine-invariant MCMC methods presented in Goodman & Weare 2010. We take the median and standard deviation of the resulting samples of the posterior distribution to be the recovered parameter value and the one-sigma error on that value.

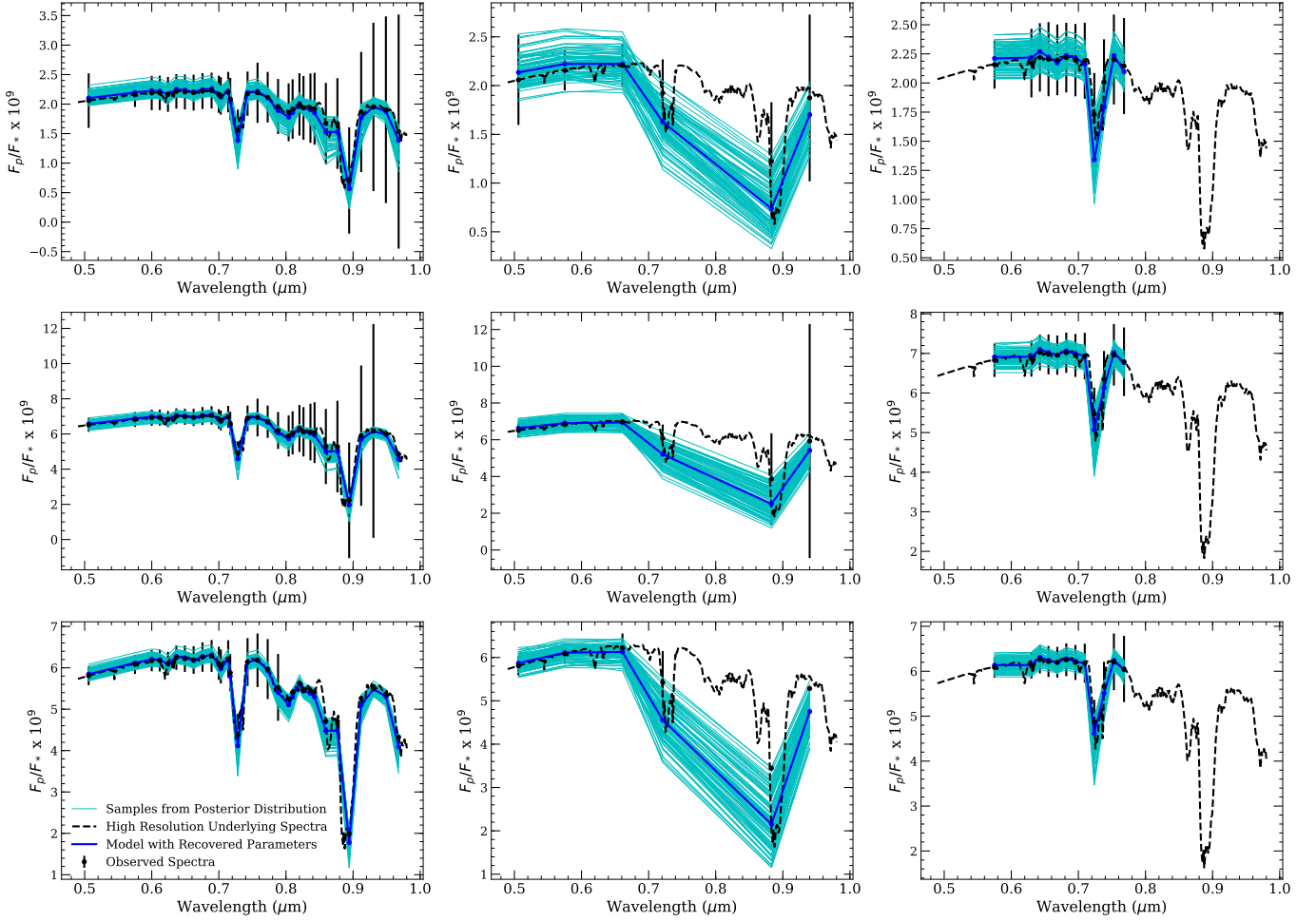


Figure 13. Example planet-star flux ratio spectra for observing cases one, two and three (**left, center, right columns**) and for the fiducial Jupiter-Sun system, 47 UMa c, and Upsilon And d (**top, middle, bottom rows**), as defined in §5.2. All spectra are computed assuming a solar metallicity spectrum from the *CoolTLusty* metallicity grid. For observing cases one and three the exposure time is 300 hours, and for observing case two the exposure time is 24 hours. For 47 UMa c and the fiducial system, the orbital phase angle is $\alpha=60^\circ$, but, for Upsilon And d, the orbital phase angle is $\alpha=90^\circ$ to minimize the wavelength coverage which falls interior to the inner working angle of the two coronagraph designs. The dashed line shows the high-resolution underlying spectra. The black dots show the clean signal that would be seen by WFIRST-CGI for each observing case in the absence of noise. Black error bars show the noise. Note that where dots do not lie along the high-resolution spectra they are representing an imaging band. The blue dots and solid line show the model given by the median parameters of posterior distribution mapped by MCMC fitting process. The cyan lines are a random sampling of 100 lines from the MCMC chain. The long-wavelength planet-star flux ratio spectra appears un-realistically well constrained considering the huge error bars. This is because the metallicity is fit as a single unit. The shorter wavelength coverage with smaller error bars is sufficient to constrain R_p and metallicity. For the fiducial system, the sizes of the error bars are larger at wavelengths below $\sim 0.65\mu\text{m}$ because the coronagraph performance is degrading as short wavelengths near the outer working angle.

Examples of the three observing cases for our fiducial system, an approximate 47 UMa c system, and an approximate Upsilon And d system are shown in Figure 13. For each observing case and

planet system, the figure shows the underlying high-resolution planet-star flux ratio spectrum, the regions of the spectrum which each observing case would sample (with corresponding uncertainties calculated using our noise model), and a random selection of models from the posterior distribution mapped by the MCMC chains.

Adopting our fiducial planet-star system, we carried out this procedure for 20 integration times between 10 and 300 hours for a grid of P_c and P_m values using the hybrid Jupiter-Neptune geometric albedo models, and for a series of metallicities using the *CoolTLusty* model. We also consider a range of orbital phases between 50 and 130 degrees at 100 hours and 300 hours using both a Lambertian phase function and the empirically measured phase function of Mayorga (2016). Results are shown in §5.3 and §5.4. In addition to these comprehensive explorations of phase and exposure time dependence using our fiducial system, we also consider the systems 47 UMa c and Upsilon And d at two planet model parameterizations, two phases, and two exposure times in all three observing cases. Results are shown in §5.5.

As noted previously, these 10- to 300-hour integration times are used to model the signal and noise on a filter-by-filter basis. They do not account for the total on-sky integration time for a whole observing case. To compare performance between the three observing cases at a fixed mission duration, then, one could take the case one performance at 100 hours and compare it to the case three performance at 300 hours, and the case two performance at 50 hours. This is only a rough estimate, though, because it will take time to return the coronagraph to full performance after switching between different imaging and IFS filters, and after switching between the two coronagraph designs intended for use with spectroscopy and the IFS.

5.3. Hybrid Model Parameter Recovery

Figure 14 shows some representative posterior distributions for the Hybrid model parameters as constrained by the three observing cases. To demonstrate the data’s ability to distinguish the two most extreme types of planet this model can represent, we superpose the posterior distributions of the fully Jovian parameterization with $P_c=1.0$, $P_m=1.0$ and the fully Neptunian parameterization with $P_c=0.0$, $P_m=0.0$. The underlying planet radius for both cases is $1.0 R_J$, as stipulated for our fiducial system. Figure 15 shows the standard deviation of the posterior distribution of each parameter as a function of exposure time, comparing all three observing cases. Considering the form of our model for SNR , we would expect all errors in Figure 15 to scale approximately with the inverse square root of the exposure time. This only appears to be the case for P_m in all three observing cases and R_p in observing case one. The fit of P_c is instead dominated by the prior which requires that it fall between 0.0 and 1.0. This falsely lowers the errors below the actual constraining power of the data at short exposure times. Looking at Figure 14, one can see that the posterior distribution spans the whole range allowed by the priors. It appears something similar is happening with R_p in observing case one based on the curve of errors versus exposure time, but the posterior distribution is clearly not encountering the bounds of the priors set on R_p (0.1 and 2.0 times R_J) when one looks at the posterior distribution in the triangle plots. The trend seen for observing case one is likely due to the fixed exposure time of 30 hours for the two imaging bands. Case three also includes an imaging band with fixed exposure time of 30 hours. It appears that as SNR in the IFS coverage lowers, the imaging bands are sufficient to keep the planet radius constrained. We note that the rate of improvement in error for P_m with additional exposure time significantly slows after ~ 150 to 200 hours for the fiducial

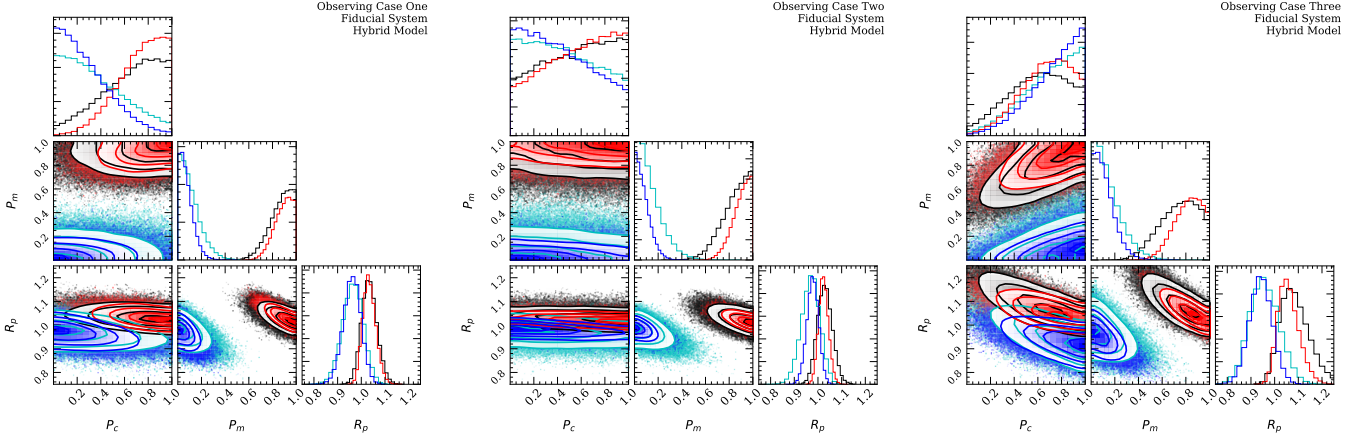


Figure 14. Triangle plots showing the posterior distributions of the Hybrid model parameters (chromophore absorption: P_c , methane-like absorption: P_m , and planet radius: R_p , in terms of Jupiter radii) for observing cases one, two, and three as defined in §5.2 (**left, center, right**). The fully Jovian-like parameterization, with $P_c=1.00$, $P_m=1.00$, is shown in red (285-hour exposure/95-hour exposure for cases one and three/case two respectively), and black (95-hour exposure/35-hour exposure). The fully Neptune-like parameterization, with $P_c=0.00$, $P_m=0.00$, is shown in blue (285-hour exposure/95-hour exposure for cases one and three/case two respectively), and in cyan (95-hour exposure/35-hour exposure). Contours mark the 0.5-sigma, 1-sigma, 2-sigma and 2.5-sigma regions, with points outside these regions represented as dots. It is clear that P_c is not constrained well in any of the observing cases. The posterior distribution of observing case three, which does not include the $0.506\text{-}\mu\text{m}$ imaging band, even excludes the correct value of P_c for the Neptunian parameterization. R_p and P_m show the usual metallicity-radius degeneracy in all three observing cases, but they are both still reasonably constrained to a sub-region of what the priors allow. These plots and subsequent triangle plots made use of the **corner** python package (Foreman-Mackey 2016).

system. These are more realistic exposure times than 300 hours in the event that all three IFS filters are used.

The results from the hybrid model fits show that WFIRST-CGI wavelength coverage and resolution recovers both the degree of methane-like absorption via the proxy parameter P_m and the radius of the planet R_p with acceptable accuracy in exposure times deemed realistic. Observing cases one and two perform best, but case three still provides some constraints, especially on planet radius. P_m is better constrained than P_c in all three observing cases. This is not surprising since the bulk of the spectral and imaging coverage overlaps the region of the planet’s geometric albedo spectrum determined by P_m . In case three, the fit of P_m is not quite as precise; degeneracies with P_c appear to have a larger effect. We find that the shorter wavelength parameter meant to be a proxy for chromophore-like absorption, P_c , is poorly constrained for our fiducial system, even at the longest exposure times. Looking at Figure 13 in the top left panel, it is clear that, for our fiducial system, the shortest wavelength imaging band falls very near the outer working angle of the coronagraph, leading to low SNR and a large error bar. In light of the large uncertainties for the $0.506\text{-}\mu\text{m}$ band, even with $P_c=1.0$, there is not a significant enough slope between the two imaging bands at $0.506\text{ }\mu\text{m}$ and $0.575\text{ }\mu\text{m}$ to constrain P_c well. Case one does better constraining P_c than case two, implying that some of the IFS coverage contributes to the fit, not just the two photometric bands. Case three, with wavelength coverage reaching only to $0.575\text{ }\mu\text{m}$, completely “mis-fits” P_c . The optimal wavelength range to constrain P_c clearly falls at wavelengths shorter than the WFIRST-CGI wavelength coverage

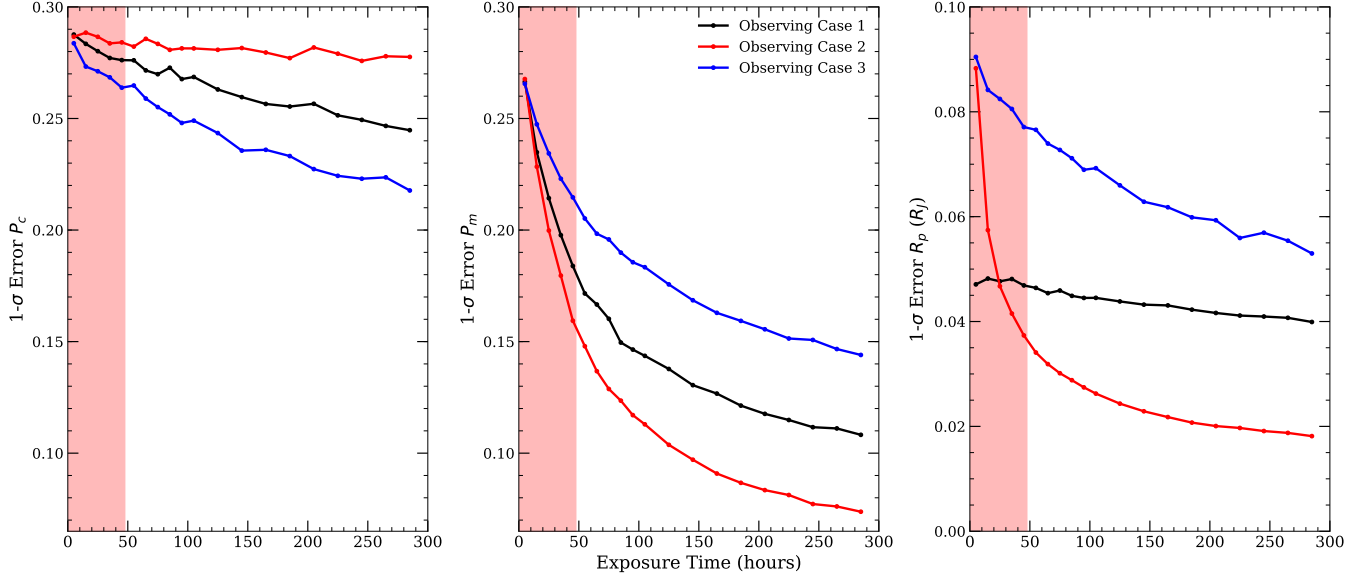


Figure 15. 68% confidence interval, or 1- σ error, of the posterior distributions for each Hybrid model parameter mapped by our MCMC methods, as a function of exposure times ranging from 5 to 300 hours. The black points and line represent observing case one, the red points and line represent observing case two, and the blue points and line represent observing case three as defined in §5.2. Red shading indicates the exposure times which are feasible for case two, so values for case two outside this red shaded region should be ignored. For this comparison, we fix planet-star system characteristics to our fiducial system and adopt the parameterization $P_c=0.5$, $P_m=0.5$ to minimize the effects of the priors biasing the width our posterior distribution. A similar study over a grid of P_c - P_m parameterizations found that the precise formulation of the geometric albedo spectra was secondary to the exposure time in determining the 1- σ errors. Errors in P_c (left) decrease roughly linearly with exposure time. Errors in P_m (middle) decrease with roughly the inverse square-root of the exposure time. Errors on R_p (right) scale differently for the different observing cases. This R_p error scaling arises because observing cases one and three include imaging bands with a fixed exposure time of 30 hours, with only IFS exposure times varying in accordance with the labels on the x-axis.

where chromophore absorption is a more dominant effect (see Figure 4), but, the performance of our fiducial system, should not be taken as indication that P_c is irrelevant in WFIRST-CGI wavelength ranges. In §5.5, focusing on 47 UMa c and Upsilon And d, it is clear that P_c can be much better constrained when the 0.506- μ m filter does not fall at such an unfavorable working angle as with our fiducial system.

The hybrid model suffers from the typical metallicity-radius degeneracy, tending to overestimate and underestimate R_p to balance out overestimates and underestimates of absorption. Recall that higher P_c values correspond to a more Jupiter-like short-wavelength behavior, meaning more chromophore absorption. Lower values of P_m correspond to more Neptune-like long-wavelength trends and, thus, more methane absorption. We expect lower P_m and higher P_c values to correspond to overestimates of R_p . Examining the panels in Figure 14, which show P_m and R_p (center of bottom row in each case), it is clear that where P_m is too low, R_p is too high and visa versa. This degeneracy is less clear between R_p and P_c , presumably because P_c has a much smaller effect at wavelengths covered by WFIRST-CGI. The P_m and R_p degeneracy does not break even for the longest exposure time of 300 hours. Despite this, R_p is limited to a relatively narrow range of values by the posterior distributions

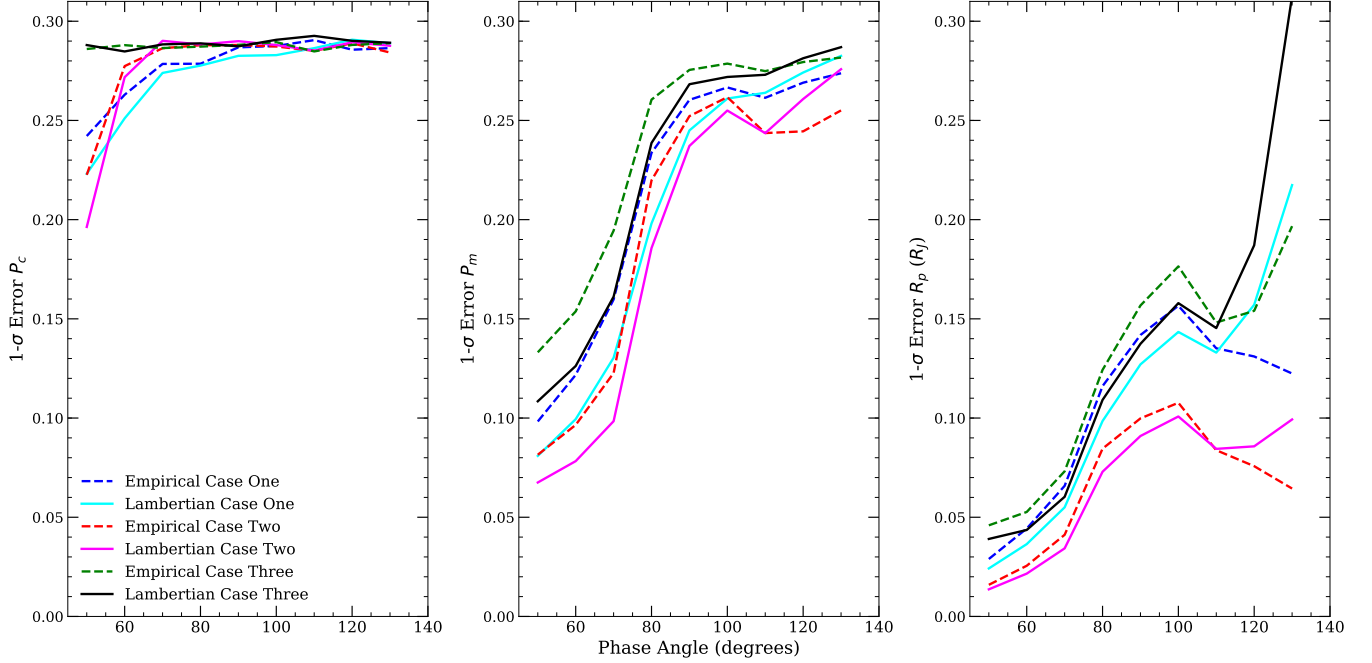


Figure 16. 68% confidence interval, or 1- σ error, of the posterior distributions for each Hybrid model parameter mapped by our MCMC methods, as a function of orbital phase. We explore phases ranging from $\alpha=40^\circ$ to $\alpha=130^\circ$, and compare the results for a Lambertian orbital phase function (solid) and the empirical Jovian phase function reported in [Mayorga et al. 2016](#) (dashed). The blue and cyan lines represent observing case one, the red and magenta lines represent observing case two, and the black and green lines represent observing case three as defined in §5.2. For this comparison we again fix planet-star system characteristics to our fiducial \sim Jupiter-Sun system and adopt the parameterization $P_c=0.5$, $P_m=0.5$. We assume a exposure times just below the point that SNR begins to improve less significantly with additional exposure time. These are 100 hours for observing cases one and three and 24 hours for observing case two. The extremely steep jump in errors around $\alpha=70-80^\circ$ is the transition where the $0.506\text{-}\mu\text{m}$ band moves from completely within the functioning working angles of the coronagraph through a region of poor performance and eventually completely exterior to the outer working angle. The dip that occurs past 90° for P_m and R_p is also likely due to IFS and imaging coverage at shorter wavelengths moving towards better working angles for coronagraph performance before the effect of significantly less illuminated area overpowers this improvement.

in all three observing cases. Case one and case two in particular attain a limit on R_p around $\pm 10\%$ at the 2.5-sigma level within the first 100 hours, and do not do much better after 285 hours. It is notable that R_p is much more precisely recovered than the other parameters in all three observing cases, even with the degeneracies illustrated by Figure 14. This is because the planet-star flux ratio has a steeper dependence on R_p than on the geometric albedo which P_c and P_m set (see eq. 1). Even taking this into account, R_p is surprisingly well constrained, considering the low SNR of the data. Planet radius can be recovered within 5 to 10% at the one-sigma level for 300-hour exposure times and our fiducial system. This is presumably due to our assumptions that the phase function, orbital phase angle, and planet-star separation are all perfectly known. All of those factors would be degenerate with R_p and incorporating uncertainties in those values would certainly increase the uncertainty in R_p .

Figure 16 shows the standard deviation of the posterior distribution of each parameter as a function of orbital phase angle, assuming both a Lambertian phase function and the empirical Jovian phase

function of [Mayorga et al. 2016](#), comparing the results for all three observing cases. The Hybrid model parameters were fixed to $P_c = 0.75$ and $P_m = 0.25$, and exposure time was fixed to 100 hours. As expected, the errors are larger for phases with less illumination, where SNR is lower for a given exposure time. The steep improvement seen for orbital phase angles less than 75° is the effect of the $0.506\text{-}\mu\text{m}$ imaging band coming into a working angle with reasonable coronagraph performance. It is still clear that observing as close to full illumination as possible while still maintaining good wavelength coverage can provide significantly better results. Because the Lambertian phase function has a higher planet-star flux ratio at phases between roughly 40° and 140° , assuming an underlying Lambertian phase function when generating and fitting the simulated spectra attains lower errors than the Jovian phase function (compare dashed and dotted lines). Differences between the two phase functions are around the same level as the one-sigma error or less, depending on the exact phase angle. Though it appears that using the wrong phase function to estimate exposure times and SNR may not have a large effect (see [Figure 9](#) and [Figure 11](#)), ignorance of the correct phase function introduces a systematic bias in planet radius hidden beneath the uncertainties of the measurements.

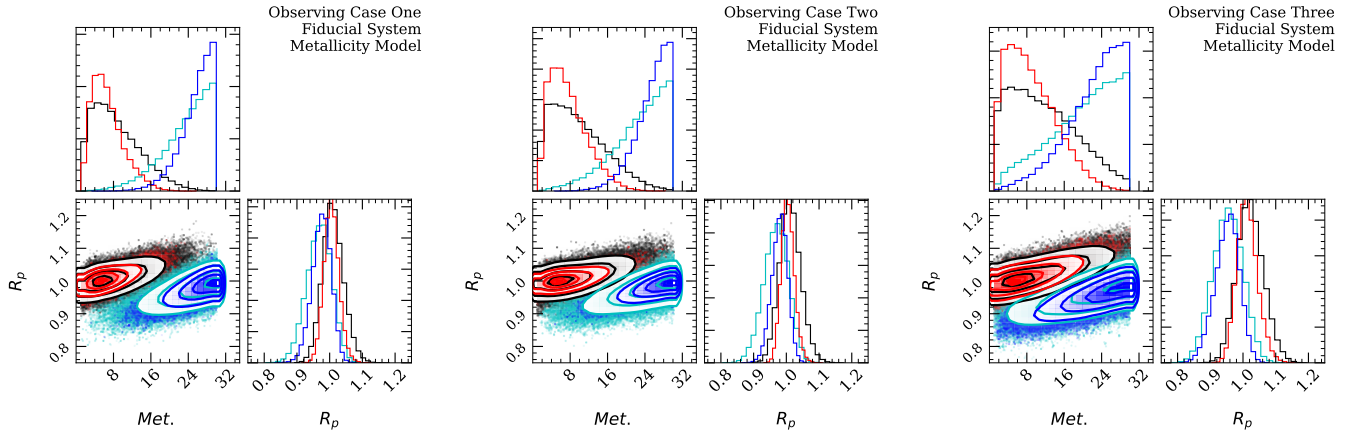


Figure 17. Triangle plots showing the MCMC sampling of the posterior distributions of the *CoolTLusty* model parameters (metallicity in terms of solar metallicity and planet radius, R_p , in terms of Jupiter radii) for observing cases one, two, and three as defined in §5.2, (**left, center, right**). The synthetic observed spectra assumed our fiducial system approximating Jupiter and the Sun observed from a distance of 11 pc at an orbital phase angle of 60° . A solar-metallicity parameterization is shown in red (285-hour exposure/95-hour exposure for cases one and three/case two respectively) and black (95-hour exposure/35-hour exposure). A 30-times solar metallicity parameterization is shown in blue (285-hour exposure/95-hour exposure for cases one and three/case two respectively) and in cyan (95 hour exposure/35 hour exposure). Contours mark the 0.5-sigma, 1-sigma, 2-sigma and 2.5-sigma regions, with points outside these regions represented as dots. The metallicity radius degeneracy is apparent, but does not prevent strong constraints on the radius of the planet. Observing cases one and two perform very similarly, while observing case three does not constrain metallicity as well. Even so, observing case three is still able to place the metallicity within the correct order of magnitude, which is the level of difference seen between Neptune and Jupiter.

5.4. *CoolTLusty*: Metallicity and Radius Recovery

Fitting the simulated observations with the *CoolTLusty* metallicity grid we find that trends in metallicity are recoverable, but only with moderate precision at the longest feasible exposure times.

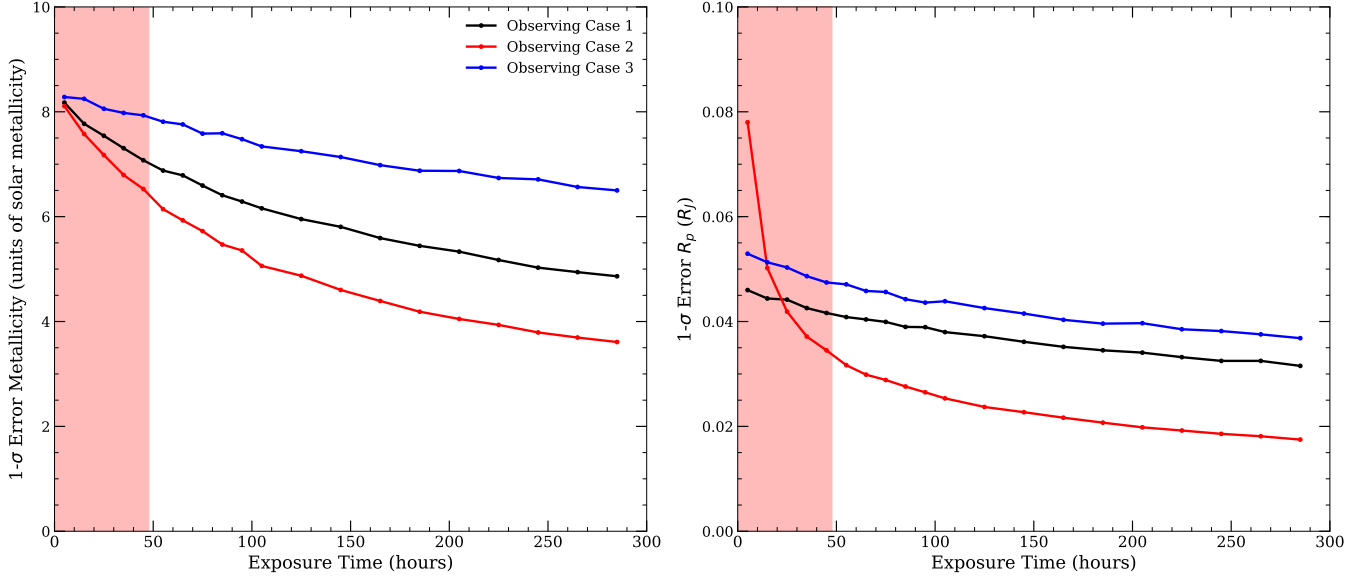


Figure 18. 68% confidence interval, or $1\text{-}\sigma$ error, of the posterior distributions for both *CoolTLusty* model parameters mapped by our MCMC methods as a function of exposure times ranging from 5 to 300 hours. All simulated observations and fits assumed a 15-times solar metallicity parameterization of the model and our fiducial system’s planet-star characteristics which approximate Jupiter and the Sun observed from a distance of 11 pc when the planet is at orbital phase angle 60° . Again, the black points and line represent observing case one, the red points and line represent observing case two, and the blue points and line represent observing case three, as defined in §5.2. The errors on metallicity do not decrease proportional to the squareroot of the observing time. This is likely due to the priors that metallicity must be between $1\times$ solar and $30\times$ solar limiting the extent of the posterior distributions, causing smaller standard deviations than the low *SNR* data at short exposure times can actually constrain on its own. Similar to the hybrid case, errors on planet radius deviate from the expected scaling with inverse squareroot of exposure time. Again, this is because observing cases one and three include photometry with a fixed exposure time, while the IFS exposure time varies in accordance with the x-axis.

Figure 17 shows representative posterior distributions for observing cases one, two and three. As for the hybrid model, we superpose the two most extreme planets that can be represented by the *CoolTLusty* metallicity grid geometric albedo model (solar metallicity exactly and thirty times solar metallicity) observed at the longest reasonable exposure time and at a shorter exposure time. Again the underlying planet radius is fixed at $1.0 R_J$ and then fit simultaneously with the metallicity. The radius-metallicity degeneracy is apparent in the sloped elliptical shape of the posterior distributions.

Looking at Figure 18, which shows the one-sigma error in all three observing cases as a function of exposure time, it is clear that the precision of the metallicity estimate does not scale with the inverse square root. At the shorter exposure times, the posterior distribution runs into the priors that metallicity must lie between 1 and 30 times solar making these errors appear smaller than they ought to be. Looking at Figure 17, it appears that at the longest exposure times for case one, the errors we’ve estimated are more closely correct, since the posterior distribution centered about 15 times solar metallicity would just fit within the priors. Despite the clear degeneracy, longer exposure times do narrow the allowed range of metallicity, improving the precision of the radius estimate. Again, we find that planet radius can be recovered surprisingly well, within $\pm 10\%$ for over ~ 100 -

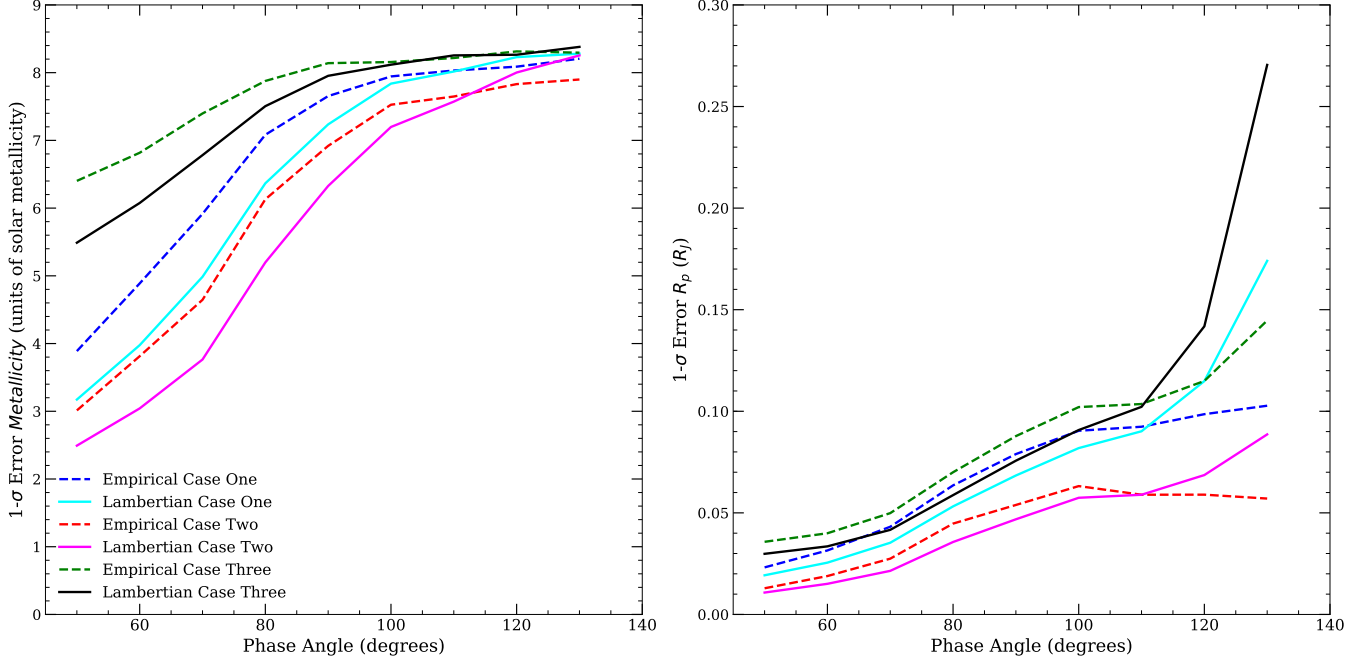


Figure 19. 68% confidence interval, or $1-\sigma$ errors, for the *CoolTLusty* metallicity geometric albedo planet model at orbital phase angles ranging from 40° to 130° . Dashed lines indicate the results for an empirical Jovian phase function, and solid lines indicate the results for a Lambertian phase function. Colors correspond to the observing cases defined in §5.2. We fix all exposure times for this figure at 100 hours for the IFS (cases one and three) and 50 hours for the imaging (case two). As planets move from 0° towards 180° , less and less of their illuminated disk is visible to the observer, causing signal to drop and errors to increase. The overall trends with phase do not seem to depend heavily on the precise phase function, but the Lambertian phase function consistently recovers parameters with smaller errors, since it predicts larger phase function values at these phase angles and thus higher *SNR*. A similar study was carried out for exposure times ranging from 5 to 300 hours, and found that the trends with phase function do not depend heavily on exposure time for their overall shape.

hour exposure times. Precision on the R_p estimate scales with the inverse square root of the exposure time for observing case two, but not observing cases one and three. Similar to the hybrid model, it appears the fixed exposure time of 30 hours for the two imaging bands included in case one and the single imaging band in case three may be enough to keep the planet radius constrained regardless of how low the *SNR* gets in the IFS coverage.

Observing cases one and two perform similarly well, especially when one tries to compare their results at exposure times which amount to an equal time on sky for the total observational strategy. Observing case three is not as effective, hardly ruling out any of the metallicities within the prior range, though it still recovers the planet radius within $\pm 20\%$.

Fixing metallicity to five times solar, we again explore the precision of the *CoolTLusty* metallicity grid parameter recoveries at orbital phases ranging from 50° to 100° and compare results for Lambertian and empirical Jovian phase functions (Figure 19). Our findings are similar to the results from fitting the hybrid model at different phases: errors shrink by over a factor of two between $\alpha=100^\circ$ and $\alpha=50^\circ$, and Lambertian phase functions predict lower errors since they overestimate planet flux. Not shown in the Figures, we conducted the same test for all twenty exposure times, and found that

errors scale in much the same way with phase at all exposure times, with only the normalization shifting up or down.

5.5. Applications to Known RV Planets

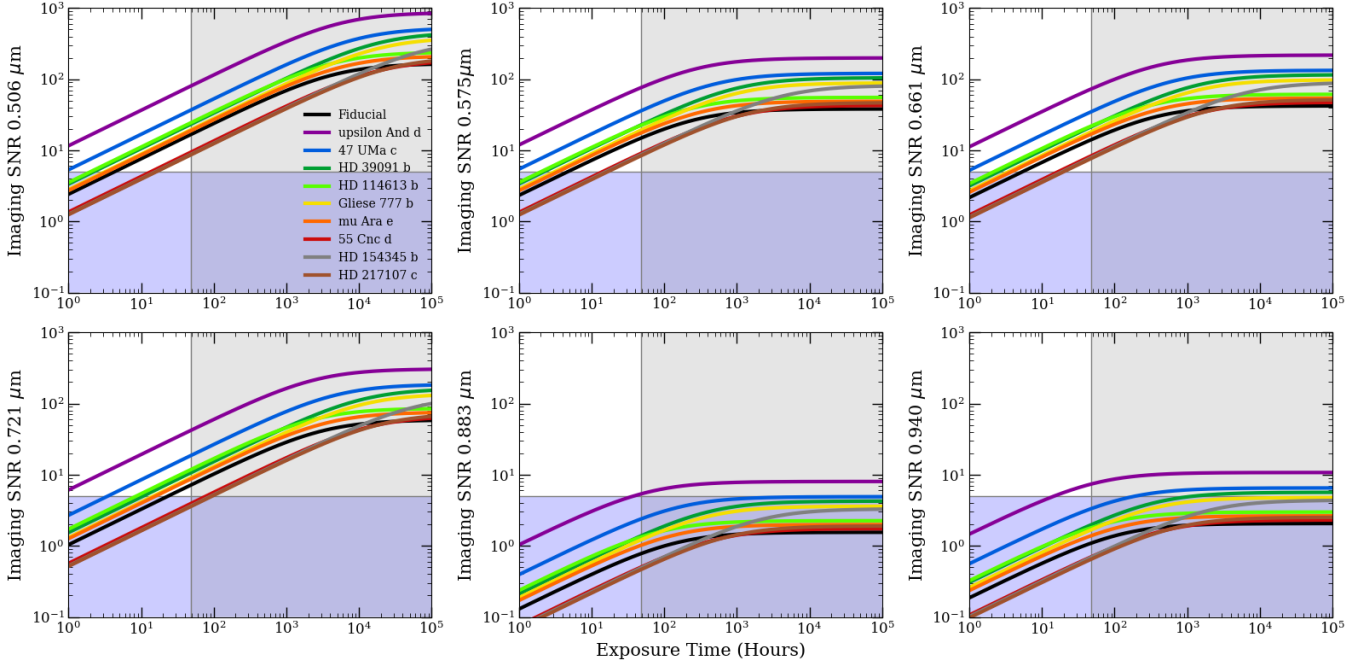


Figure 20. *SNR* dependence on exposure time computed for known RV planets in the imaging bands (labeled on the y axis of each panel). All *SNR* calculations assume a Jovian geometric albedo spectrum, edge-on orbit, and orbital phase angle of 60° . We include our adopted fiducial system approximating Jupiter and the Sun observed from a distance of 11 pc (black). The gray shaded region indicates exposure times above 48 hours. The purple shaded region indicates *SNR* below five. Bands centered at $0.506 \mu\text{m}$, $0.575 \mu\text{m}$, $0.661 \mu\text{m}$, and $0.721 \mu\text{m}$ attain useful *SNRs* for many systems within 48 hours. The longest wavelength imaging bands centered at $0.883 \mu\text{m}$ and $0.94 \mu\text{m}$ do not yield *SNR* above five for any system other than 47 UMa c.

Similar to Figures 9 and 10, Figures 20 and 21 depict the results of calculations of *SNR* as a function of exposure time for the central wavelength of the IFS filters and for the imaging filters, but now using planet radii, planet-star separations, stellar types, stellar magnitudes, and observing distances which correspond to known RV planets (see Table 2 in the Appendix for a list of planet-star system parameters and an explanation of their selection). Our fiducial system is also plotted for comparison. We assume all planets are observed at the phase $\alpha=60^\circ$ and use the empirical Jovian phase function of Mayorga et al. 2016. Planets do not appear in plots where they fall outside the working angles of the appropriate coronagraph for either imaging (the HLC) or spectroscopy (the SPC). Out of these known RV targets, 47 UMa c attains close to the highest *SNR*, and is observable across all imaging and IFS bands. Upsilon And d attains higher *SNR*, but is not visible in the longer wavelength IFS bands. A number of other known planets attain *SNR* just slightly above the fiducial system for which the previous tests were carried out (§5.1, §5.3, and §5.4).

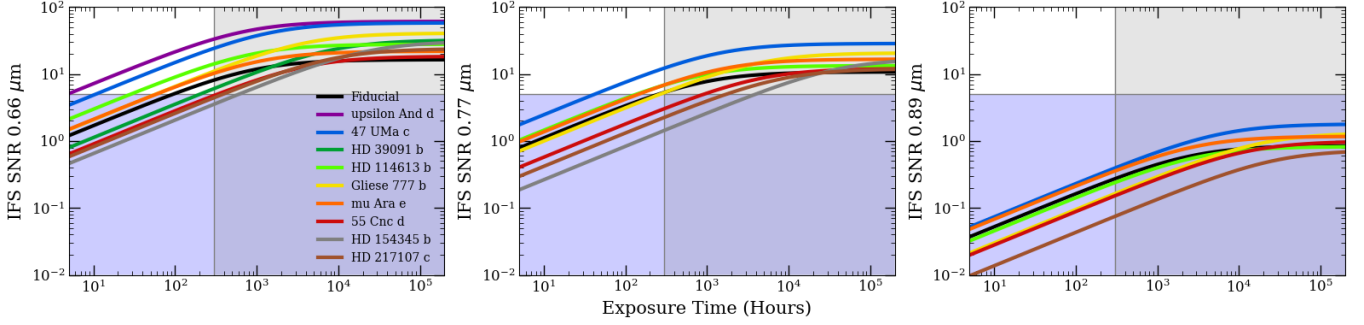


Figure 21. *SNR* dependence on exposure time computed for known RV planets and our adopted fiducial system (black) at the center of the three IFS bands (**Left:** $0.66\ \mu\text{m}$, **Center:** $0.77\ \mu\text{m}$, **Right:** $0.89\ \mu\text{m}$). For simplicity, calculations assume all planets have a Jovian geometric albedo spectrum, edge-on circular orbits, and are observed when the planets are at an orbital phase angle of 60° . The gray shaded region indicates exposure times above 300 hours. The purple shaded region indicates *SNR* below 5. Upsilon And d and HD 39091 b are shown only in a subset of panels because, at longer wavelengths, they move inside the inner working angle of the SPC coronagraph. These *SNR* calculations demonstrate the appeal of observing case three (defined in §5.2), which includes a single IFS filter with 18% full-width between the $0.66\text{-}\mu\text{m}$ and $0.77\text{-}\mu\text{m}$ filters, rather than including all three. Unless targets closer by than the known RV planets are discovered, the longest wavelength coverage of the IFU will not attain reasonable *SNR* at $R=50$.

To quickly evaluate the potential for observing 47 UMa c and Upsilon And d, synthetic observations were generated for all three observing cases at 60° and 90° , at 30 and 300 hours for IFS, and 10 and 24 hours for imaging, and at the extreme ends of our planet model parameterizations: a Neptune-like planet with $P_c=0.0$, $P_m=0.0$, and a Jupiter-like planet with $P_c=1.0$, $P_m=1.0$, a solar-metallicity planet, and a 30 times solar-metallicity planet. In all cases the radius was kept to $1.0\ R_J$. The posterior distributions for 47 UMa c observed at $\alpha=60^\circ$ and Upsilon And d at $\alpha=90^\circ$ are shown in the Appendix in Figures 25 and 26, respectively. Overall, the findings from the fiducial case seem to hold: R_p is well constrained and rough trends with the degree of methane absorption measured via P_m or metallicity depending on the model are recovered. P_c is much better constrained than for the fiducial system, presumably due to the more favorable working angle of the $0.506\text{-}\mu\text{m}$ imaging band. Similar to the findings for our fiducial system, observing cases one and two perform reasonably well, while observing case three is not as effective for the Hybrid model case. Upsilon And d moves inside the inner working angle of the telescope even when observed at the widest separation possible for a circular edge on orbit: $\alpha=90^\circ$ (see bottom row of Figure 13). This has a particularly negative impact on the performance of case two, where measurements are only available in four out of six imaging bands.

In light of these findings for Upsilon And d and 47 UMa c and the numerous other systems which achieve *SNR* levels comparable to or superior to our fiducial system seen in Figure 20 and Figure 21, it is sensible to take the previous explorations of the Hybrid model and *CoolTLusty* metallicity grid as a conservative assessment of WFIRST-CGI performance, provided the final adopted mission architecture is similar to one of the three observational strategies presented here. Altering wavelength coverage and resolution significantly will have a large effect on results.

5.6. The Effect of Phase-Curve Wavelength Dependence

Previous studies have pointed out that gas giant planets exhibit a change in color with phase. In our previous explorations, we simplified by assuming a wavelength-independent phase function across the WFIRST-CGI coverage. To test the impact of this simplification, we simulated WFIRST-CGI observations for the three observing cases assuming the fiducial Jupiter-Sun system observed from a distance of 11 parsecs, a planet geometric albedo spectrum with $P_c=0.5$, and $P_m=0.5$, and a wavelength-dependent Rayleigh scattering phase curve generated using the methods described in §4.1. For observing case one we incorporated noise assuming 150 hour exposure times for each IFS filter, for observing case two we assumed exposure times of 48 hours for each imaging filter, and for observing case three we assumed an exposure time of 300 hours for the single IFS filter. We then fit the three cases in the same manner described in §5.2, assuming a fixed value of Mayorga 2016’s empirical phase function evaluated at $\alpha=60^\circ$ regardless of wavelength.

In all three observing cases, the planet radius was recovered within 8% to 10%. This is similar to the results found fitting simulated data with the wavelength-independent empirical phase curve at the same exposure times. P_c was poorly constrained in all three observing cases, though case one did recover a value of 0.48 ± 0.28 at the $2.5\text{-}\sigma$ level. P_m was reasonably well constrained, with precision about three times better than P_c in all three observing cases.

This simple test hints that, for the quality of data expected with WFIRST-CGI, our ignorance of the wavelength-dependence and precise shape of planet phase curves may not be a problem. This is especially true if exoplanets observed with WFIRST-CGI are similar to Jupiter in their scattering properties. The shaded blue region in Figure 5 demonstrates the range of values a Rayleigh scattering phase curve can take on, depending on the scattering albedo. Around $\alpha=60^\circ$, the Rayleigh scattering phase function can range from ~ 0.42 to ~ 0.5 depending on the scattering albedo. The fixed value of the empirical phase curve is near the upper end of the Rayleigh range, but the Lambertian phase curve is quite a lot higher. It should be noted that real planets are seen to have more extreme color variations than the analytic Rayleigh scattering phase curves can explain.

6. DISCUSSION

6.1. WFIRST-CGI Exposure Times

The precise combination of imaging and IFS filter coverage which will fly with WFIRST-CGI is still an ongoing topic of discussion. Our results relating SNR to exposure times provide strong motivation for exploring the science possible with only a subset of the IFS coverage, leaving off the longest wavelengths, and for considering the potential of narrow band photometry alone. As mentioned within §5.1, the model we implemented for WFIRST-CGI noise would change if we consider the case that observations are post-processed with a matched filtering algorithm (Kasdin et al. 2003) rather than reference differential imaging. This could provide improvement over the SNR -exposure time relations presented here. Other instrument and engineering advancements, such as alternative ways of removing cosmic rays, may also influence instrument throughput and favorably improve SNR .

The long exposure times will limit the total number of planets that can be characterized by the mission. This will make it difficult to conclusively identify trends with planet size, stellar host type, planet-star separation and metallicity, but it may still be possible to uncover hints and rule out some theories depending on what is observed.

6.2. Applicability of our two Geometric Albedo Models

The hybrid model addresses two primary questions. First, will WFIRST-CGI be able to distinguish a Jupiter-like planet from a Neptune-like planet of the same size? Second, will WFIRST-CGI be able to recognize chromophore-like absorption at short wavelengths or methane-like absorption at long wavelengths? Our findings indicate that the chromophore absorption will be recognizable only if it is near the levels seen on Jupiter and the target system allows SNR around the levels of 47 UMa c and Upsilon And d. Differences in longer wavelength methane-like absorption on the order of that between Jupiter and Neptune will be distinguishable for many of the known-RV planets most likely to be selected as targets.

The *CoolTLusty* metallicity grid addresses the question: assuming known haze/cloud properties, can we measure the metallicity of WFIRST-CGI targets? Our findings indicate that with high enough SNR ($SNR \sim 12, 11$ at IFS $0.66\text{-}\mu\text{m}$ and $0.77\text{-}\mu\text{m}$ band centers), which should be just barely achievable at the longest WFIRST-CGI exposure times (~ 300 hours) for our fiducial system, qualitative trends in metallicity should be recognizable. Even without the IFS, the imaging-only observing case can also distinguish between solar and 30 times solar metallicities.

Based upon our fiducial \sim Jupiter-Sun system, 47 UMa c, and Upsilon And d, both the hybrid Jupiter-Neptune model and the *CoolTLusty* metallicity grid would be useful for fitting actual WFIRST-CGI data. The hybrid model could be further improved by only including the P_c parameter for observing cases which extend to shorter wavelengths with sufficient SNR , like Upsilon And d and 47 UMa c. Because it is possible that planets will have higher metallicities than $30\times$ solar, it would be worthwhile to expand the metallicity grid up to at least the levels of Neptune and Uranus. Fit results for both models demonstrate that a rough indication of the metallicity based upon the $0.65\text{-}\mu\text{m}$ to $0.90\text{-}\mu\text{m}$ planet-star flux ratios should be possible for WFIRST-CGI targets, especially with observing cases one and two. They can both confidently differentiate between extreme models, but lack precision to uncover subtle trends. Planet radius should be well recovered within $\pm 10\%$ for observing cases one and two with both the hybrid model and the *CoolTLusty* metallicity grid. This precision for the radius assumes a well-understood phase function and well-known Keplerian orbital parameters of the target planet.

7. SUMMARY AND CONCLUSIONS

In this paper we examined the potential of WFIRST-CGI observations to provide information about extrasolar giant planets. To do this, we constructed two simple models for a giant exoplanet’s geometric albedo spectra and paired these with the empirical Jovian phase curve to compute likely observed WFIRST-CGI planet-star flux ratio spectra. We then used the parameterized semi-analytic noise model of [Nemati et al. \(2017\)](#) to add noise for three different observing scenarios combining subsets of the imaging filters and IFS coverage. We presented calculations of the signal-to-noise ratio for given exposure times for known RV planets, and demonstrated the general dependence on relevant star-planet system parameters: separation, planet radius, distance from observer, orbital phase, and exozodi level. We carried out a suite of MCMC fits on simulated data to evaluate the precision and accuracy with which input geometric albedo model parameters and planet radius could be recovered for three different observing scenarios. We evaluated the effect of assuming a simple wavelength-independent phase function when fitting data generated with a wavelength-dependent phase function for the same three observing cases. Our important findings are summarized in the following bulletized list:

- The imaging bands can attain SNR 's of 5-100 within 48 hours for the 0.506- μm , 0.575- μm , 0.661- μm , and 0.721- μm bands for planet-star system characteristics consistent with known RV planets. The 0.883- μm and 0.940- μm bands only attain an SNR of 5 or greater for the most favorable cases with large planet radii, small separations, and a nearby planet-star system.
- Even for the most promising known RV planets (e.g. 47 UMa c and Upsilon And d), reasonable exposure times for the IFS will be hundreds of hours, limiting the number of targets observed (likely to only one at the longest wavelengths). This is consistent with previous work (Traub et al. 2016).
- Observing systems that are nearby improves SNR through multiple avenues: in addition to increasing the observed photon flux (which scales with the inverse of distance squared), this allows the target planet to be observed at a smaller separation or closer to full phase without falling interior to the IWA.
- Observing at a favorable orbital phase angle can lead to \sim factor of two improvements in SNR for both the IFS and imaging, depending on the exact wavelength and band width. This translates into the one-sigma errors on recovered parameters shrinking by a factor of 2 to 4, depending on whether the parameter uncertainties are data-dominated or prior-dominated.
- The main challenge facing the IFS is at the longer wavelengths. Some of the most interesting features occur at these wavelengths, but a variety of factors conspire to give this portion of the spectrum an order of magnitude lower SNR for any given exposure time. Many targets move interior to the IWA at those wavelengths, rendering them completely unobservable. Or, if they are observable, targets have lower SNR due to the deep and wide spectral features, plunging quantum efficiency, and increasing noise contributions from the growing PSF size.
- Pairing photometry in WFIRST-CGI imaging filters with IFS coverage may significantly improve constraining power, particularly at the shortest wavelengths where the IFS does not function and at the longest wavelengths where the IFS struggles to achieve sufficient SNR .
- Observing planets with radii more similar to Neptune than Jupiter will likely be limited to the nearest stars (within less than 9 parsecs). Even then, if they exhibit significantly lower geometric albedos than those considered here, they may remain out of sight.
- Obtaining an SNR of 5 in the IFS at the bottom of the 0.88- μm methane feature will not be possible except for separations and radii which are implausible based upon known RV targets.
- The level of exozodi in a system does not have a strong impact on SNR when observing Jupiter-sized planets at 5 AU, even up to 200 exozodis.
- For planets similar to the known RV list presented in Table 2, constraining both planet radius and the level of methane absorption is feasible if phase functions and other orbital parameters are known.
- Our hybrid Jupiter-Neptune model places constraints on the methane-like absorption parameter P_m with around $\pm 20\%$ accuracy at the 2.5 sigma level. This is sufficient to differentiate between Jupiter and a Neptune-like planet with Jupiter's radius.

- The wavelength coverage of WFIRST-CGI IFS is not optimal for constraining the degree of chromophore-like absorption parameterized with P_c , but this information can be recovered from imaging observations if SNR ’s around 5-10 can be attained in the short-wavelength imaging bands at $0.506 \mu m$ and $0.575 \mu m$.
- Our *CoolTLusty* metallicity grid indicates that trends in metallicity are recoverable assuming other atmosphere properties are fixed, but only with moderate precision of ± 5 times solar metallicity at the one-sigma level, and ± 10 times solar metallicity at the 2.5-sigma level for the longest feasible exposure times with observing cases one and two.
- Using both models for geometric albedo we find that planet radius can be recovered within less than $\pm 0.1 R_J$ at the 2.5-sigma level. We note that this precision will degrade somewhat when uncertainties in orbital phase angle and orbital phase function are fully accounted for.
- A Lambertian phase function and the observed Jovian phase function predict differences on a level that necessitates marginalizing over uncertainties both in orbital phase and in the character of the phase function itself.
- Ignoring the wavelength-dependence of a Rayleigh-scattering atmosphere’s phase curve does not dominate the uncertainties in fits to spectra of the typical quality expected for WFIRST-CGI.

It is clear that the WFIRST-CGI project pushes the boundaries of our current technology, making it a vital step forward in space-based high-contrast imaging of exoplanets. While data seem likely to be of limited quantity and only modest SNR , prospects seem promising for obtaining new insights into the characteristics of the handful of giant extra-solar planets that will be observed in detail.

The authors would like to acknowledge support for this research under their NASA WFIRST-SIT award # NNG16PJ24C, NASA Grant NNX15AE19G, and NASA JPL subcontracts no. 1538907, 1529729, 1513640 & 1534432-B-4.25. We are grateful to Bijan Nemati and Jeremy Kasdin for insightful conversations, and we thank Sergei Yurchenko and Alex Howe for help with the ExoMol methane database.

APPENDIX

A. NOISE MODEL DETAILS

A.1. *Quantum Efficiency, Excess Noise Factor, and other losses in EMCCDs*

We adopt a wavelength-dependent detector quantum efficiency (QE), which falls off in sensitivity towards redder wavelengths in approximate accordance with [Nemati \(2014\)](#); [Harding et al. \(2016\)](#):

$$\eta_{det}(\lambda) = \begin{cases} 0.87, & \lambda < 0.7 \mu m \\ 0.87(1.0 - (\lambda - 0.7)/0.32)) & \lambda > 0.7 \mu m . \end{cases} \quad (A1)$$

We then multiply η_{det} by additional losses due to hot pixels (0.98), losses due to cosmic rays (0.9), and a net charge transfer efficiency (0.865), all values taken from [Nemati et al. \(2017\)](#). We assume the IFS will operate in photon-counting mode, so we also multiply by photon-counting efficiency (0.9). The effective value of η is thus reduced from $\sim 90\%$ to $\sim 60\%$ for the IFS and $\sim 70\%$ for imaging at

wavelengths shorter than $0.7 \mu\text{m}$. All photonic terms, including zodiacal and planet light, will be reduced by this full value of η .

For this paper we assume that, while imaging, the EMCCD will operate in analog gain mode, not photon-counting mode. The stochastic nature of the amplification process in EMCCDs results in an excess noise factor, or ENF , which multiplies contributions to r_n from planet light, speckles, zodiacal light, dark current, and clock-induced charge by an amount proportional to the actual rate of the signal. The ENF asymptotes to a maximum value $\sqrt{2}$ (Denvir & Conroy 2003), so we conservatively assume an ENF of root two in all our imaging SNR calculations.

A.2. Electronic Effects: Dark Current, Read Noise, and Clock-Induced Charge

Our model includes noise from electronic sources originating in the detector. The dark current variance rate into the signal region is given by:

$$r_{\text{dark}} = i_d N_{\text{pix}}^{\text{detector}}, \quad (\text{A2})$$

where i_d is the level of dark current present in the detector with units of $e^-/\text{s}/\text{pixel}$. Over the course of the mission, the levels of dark current are expected to rise as radiation damage degrades the detector (Harding et al. 2016). Preliminary tests predict a factor of two increase in dark current levels from the beginning of mission to the end of the mission.

For an IFS, we calculate the number of pixels involved in the signal region, $N_{\text{pix}, \text{detector}}$, according to:

$$N_{\text{pix}}^{\text{detector}} = N_{\text{lens}} \left(N_{\text{spec}} \frac{\lambda}{\lambda_c} \right)^2, \quad (\text{A3})$$

where N_{spec} is the number of pixels in each $\Delta\lambda$ in the spectral dimension, N_{lens} is the number of lenslets that the signal falls on, and λ_c is the wavelength at which the system has been designed to be Nyquist sampled. The IFS will be designed to have constant dispersal, making N_{spec} independent of wavelength. Taking our fiducial values we have:

$$N_{\text{pix}}^{\text{detector}} \sim 20 \left(\frac{\lambda}{\lambda_c} \right)^2. \quad (\text{A4})$$

Imaging signal regions contain ~ 4 times less pixels, scaling instead as:

$$N_{\text{pix}}^{\text{detector}} \sim 5 \left(\frac{\lambda}{\lambda_c} \right)^2. \quad (\text{A5})$$

Clock-induced charge, associated with high-frequency clocking needed for rapid readout rates, are accounted for as:

$$r_{\text{cic}} = q_{\text{cic}} \frac{N_{\text{pix}}^{\text{detector}}}{t_{\text{fr}}}, \quad (\text{A6})$$

where q_{cic} is the average amount of clock induced charge in units of $e^-/\text{frame}/\text{pixel}$, and t_{fr} is the maximum length for a single exposure in the observing sequence in units of seconds. Generally t_{fr} is chosen to limit the probability of cosmic ray hits to the detector during an exposure.

Levels of both dark current and clock-induced charge will be reduced by the losses from hot pixels, cosmic rays, charge transfer efficiency and, in the case of the IFS, photon-counting efficiency, similar to the photonic sources.

The read noise is described by:

$$r_{read} = i_r \frac{N_{pix}^{detector}}{t_{fr}} , \quad (A7)$$

where i_r is the effective read noise in units of $e^-/\text{frame}/\text{pixel}$. i_r is really the more conventional understanding of CCD read noise σ_{e^-} , attenuated by the electron multiplying register's gain stages, G_{EM} . For the detector baselined for WFIRST's coronagraph σ_{e^-} is on the order of tens of $e^-/\text{frame}/\text{pixel}$ and G_{EM} is on the order thousands, giving an effective read noise much less than one.

In the case of photon-counting mode, levels of read noise will be additionally reduced by the photon-counting efficiency, but not the cosmic rays, hot pixels, and charge transfer efficiency. This is because it enters into the data after all the gain stages.

A.3. Throughputs

We must specify three separate throughputs because a coronagraph affects planet light (τ_{pla}), zodiacal light (τ_{zod}), and speckle light (τ_{spe}) differently. Point sources, extended sources, and residual scattered light travel different optical paths within the instrument. Obscuration due to the struts/secondary mirror, the losses from reflections, losses due to the filter, and losses due to the polarizer affect all three throughputs. The planet throughput must also account for the occulting mask and PSF core throughput, combined into the term $\tau_{core} = \frac{\tau_{occ}}{\tau_{PSF}}$. This gives the expression for planet throughput:

$$\tau_{pla} = \tau_{core} \tau_{obs} \tau_{ref} \tau_{fil} \tau_{pol} , \quad (A8)$$

where τ_{obs} is the throughput accounting for obscuration from struts and secondary mirror, τ_{ref} is the throughput accounting for losses from reflections, τ_{fil} is the throughput accounting for losses due to the filter, and τ_{pol} is the throughput accounting for losses due to a polarizer. Note that the core throughput and occulting throughput will depend on the working angle at which the planet falls on the detector. To incorporate this working angle dependence into our model, we employ coronagraph performance models from Krist et al. (2016) shown in Figure 1. When computing rates for the IFS we use the SPC table produced in June 2017, and when computing rates for the imager we use the HLC table created in December 2016.

The zodiacal light is a diffuse source, so it need only account for the occulting mask without considering core throughput:

$$\tau_{zod} = \tau_{occ} \tau_{obs} \tau_{ref} \tau_{fil} \tau_{pol} . \quad (A9)$$

The reason for this difference in diffuse sources is that any light scattered *out* of the signal area due to core throughput limitations will be made up for by light scattered *into* the signal area from another part of the sky. This throughput thus assumes that the zodiacal light is of uniform brightness across the field of view. That assumption is likely wrong, but there is little alternative since exact structures of dust disks are not known.

The speckle throughput leaves off losses due to the occulter and core throughput, since the speckles arise from scattered light within the optics. It is, thus, defined as:

$$\tau_{spe} = \tau_{obs} \tau_{ref} \tau_{fil} \tau_{pol} . \quad (A10)$$

A.4. Planet Count Rate

The planet count rate is the product of the collecting area A_{PM} , planet throughput τ_{pl} , quantum efficiency η , and the incoming flux density of photons from the planet. This flux density is simply

the planet-star flux ratio given by eq. (1) multiplied by the stellar flux. To model stellar flux we scale spectra of various main sequence stellar types at zero magnitude to the desired absolute V-band magnitude, and then account for observing distance. This is similar to the methods employed by Nemati et al. (2017). For the IFS the calculation is as follows:

$$F'_{\star,\lambda} = F_{0,\lambda} \left(\frac{10pc}{d_{obs}} \right)^2 10^{-M_*/2.5} \frac{\lambda^2}{hcR}, \quad (\text{A11})$$

where $F_{0,\lambda}$ is the standard zero magnitude V band flux of the desired spectral type, d_{obs} is the distance to the observed system, M_* is the absolute magnitude of the host star in V band, λ is the wavelength of light, h is Planck's constant, and c is the speed of light. We take advantage of the constant resolving power $R = \frac{\lambda}{\Delta\lambda}$ of the IFS to convert the specific flux density to a photon flux. To compute rates for the imager, we assume a very high resolving power and carry out the same calculation as the IFS, now summing across the spectral bins which fall within the imaging band.

A.5. Zodiacal and Exozodiacal Count Rate

We include background light from zodiacal and exozodiacal dust following Robinson et al. (2016)'s adaptation of Stark et al. (2014). Stark et al. (2014) demonstrated that a constant V-band surface brightness of $M_{z,V} = 23$ mag arcsec⁻² provides a reasonable representation of zodiacal light ignoring the true variation with ecliptic latitude and longitude first presented by Levasseur-Regourd & Dumont (1980). The count rate from zodiacal light is:

$$r_z = A_{PM} \tau_{zodi} \eta \Omega \frac{F_{\odot,\lambda}(1AU)}{F_{\odot,V}(1AU)} F_{0,V} 10^{-M_{z,V}/2.5} \frac{\lambda^2}{hcR}, \quad (\text{A12})$$

where Ω is the angular size of the photometry aperture area in arcsec², $M_{z,V}$ is the magnitude of zodi surface brightness, $F_{\odot,\lambda}(1AU)$ is the specific flux density of the Sun at a distance of 1 AU, $F_{\odot,V}(1AU)$ is the flux density of the Sun at 1 AU in V band, and $F_{0,V}$ is the flux density of a zero magnitude star in V band.

Stark et al. (2014) define a ‘‘zodi’’ as the surface brightness of an exozodiacal disk a distance of 1 AU from a solar twin. This has exozodi surface brightness $M_{ez,V} = 22$ mag arcsec⁻², approximately double the local zodi since the observer receives reflected light from above and below the midplane of the system. The count rate from a system with N_{ez} zodis of dust, for a planet a AU from its star, observed from a distance d_{obs} is given by:

$$r_{ez} = A_{PM} \tau_{zodi} \eta \Omega N_{ez} \left(\frac{10pc}{d_{obs}} \right)^2 \left(\frac{1AU}{a} \right)^2 F'_{\star,\lambda}(1AU) \frac{F_{0,V} 10^{-M_{ez,V}/2.5}}{F_{\odot,V}(1AU)}, \quad (\text{A13})$$

where $F'_{\star,\lambda}(1AU)$ is the photon flux density a distance of 1 AU from the star (e.g., put 1 AU into equation A5 for d_{obs}). Since Ω will scale with λ^2 both r_z and r_{ez} are proportional to λ^4 .

A.6. Speckle Count Rate

Following the work of Krist et al. (2016) and Nemati et al. (2017) we adopt the speckle count rate:

$$r_{sp} = A_{PM} \tau_{sp} \eta F'_{\star,\lambda} C_{raw} I_{pk} N_{pix}^{model}. \quad (\text{A14})$$

The coronagraph raw contrast, C_{raw} , is the azimuthally-averaged, smooth background contrast achieved at a given radius on the detector. The normalized peak pixel value, I_{pk} , is the reflected light count within the brightest pixel at a given radius on the detector. Both values are taken from tables produced by [Krist et al. 2016](#), the same models shown in Figure 1. We multiply I_{pk} by N_{pix}^{model} , conservatively assuming the worst case scenario for the speckle light: that every pixel in the signal area has the peak value at that radius. N_{pix}^{model} is a value distinct from the number of pixels in the signal region on the actual detector, $N_{pix}^{detector}$, because the tables are created assuming a different pixel size than may eventually be used on the real instrument.

Parameter	Fiducial Value
f_{pp}	0.1
A_{PM}	4.449 (m ²)
D	2.38 (m)
τ_{obs}	0.83
τ_{ref}	0.474
τ_{fil}	0.90
τ_{pol}	1.0
τ_{occ}	see Figure 1
τ_{core}	see Figure 1
I_{pk}	see Figure 1
C_{raw}	see Figure 1
Θ_{IWA}	2.6 (λ/D)
Θ_{OWA}	9.0 (λ/D)
η	~ 0.65 , see §A.1
ENF	$\sqrt{2}$
R	50.0
N_{spec}	2.0
N_{lens}	5.0
$N_{pix}^{detector}$	imaging: 5, IFS: 20
λ_c	0.6 μm
i_d	2.1×10.0^{-4} ($e^-/\text{pixel}/\text{sec}$)
i_r	1.0×10.0^{-4} ($e^-/\text{pixel}/\text{frame}$)
q_{cic}	0.01 ($e^-/\text{pixel}/\text{frame}$)
t_{fr}	30 (sec)
$F_{0,V}$	3.6×10^{-8} (W m ⁻² μm^{-1})
$F_{\odot,V}(1AU)$	1.86×10^3 (W m ⁻²)
$M_{z,V}$	-23.0 (magnitudes arcsec ⁻²)
$M_{ez,V}$	-22.0 (magnitudes arcsec ⁻²)
$F_{\odot,\lambda}(1AU)$	from Kurucz (2005) ^a

^a<http://kurucz.harvard.edu/stars/Sun/fSunallp.1000resam251>

Table 1. Summary of adopted fiducial model parameters, including instrument parameters and astrophysical parameters.

Planet Name	Primary Apparent V-band Magnitude	Distance to system (pc)	Primary Stellar Type	Semi-major Axis (au)	Planet Radius (R_J)
Fiducial System	5.04	11.0	G2V	5.0	1.0
upsilon And d	4.1	13.5	F9V	2.52	1.15
47 UMa c	5.03	14.1	G1V	3.57	1.27
HD 39091 b	5.65	18.3	G0V	3.35	1.11
HD 114613 b	4.85	20.7	G3IV	5.31	1.28
Gliese 777 b	5.73	15.9	G7IV-V	3.97	1.21
mu Ara e	5.12	15.5	G3IV-V	5.34	1.21
55 Cnc d	5.96	12.3	G8V	5.47	1.16
HD 154345 b	6.76	18.6	G8V	4.21	1.23
HD 217107 c	6.17	19.9	G8IV	5.33	1.18

Table 2. Selection of the planets taken by Traub et al. (2016) from the Exoplanet Orbit Database at Penn State University. Their full sample of 127 targets was selected by downloading “RV planets” on Sept. 12, 2015, eliminating stars with missing distances or V magnitudes, and keeping only systems with a planet-star separation greater than 0.040 arc sec. Radii are assigned by assuming that the measured $m \sin i$ value is the approximate mass of the planet, and using an empirical mass-radius relation. This table includes only those systems which are shown in Figure 20 and Figure 21. They are loosely chosen to be those targets likely to attain the highest SNR with WFIRST-CGI, i.e. systems closer to Earth, and to fall within the working angles of the coronagraphs at most wavelengths. There was not a steep drop off in SNR for other systems on the full list of 127 planets. The list was truncated only for visual clarity in Figure 20 and Figure 21.

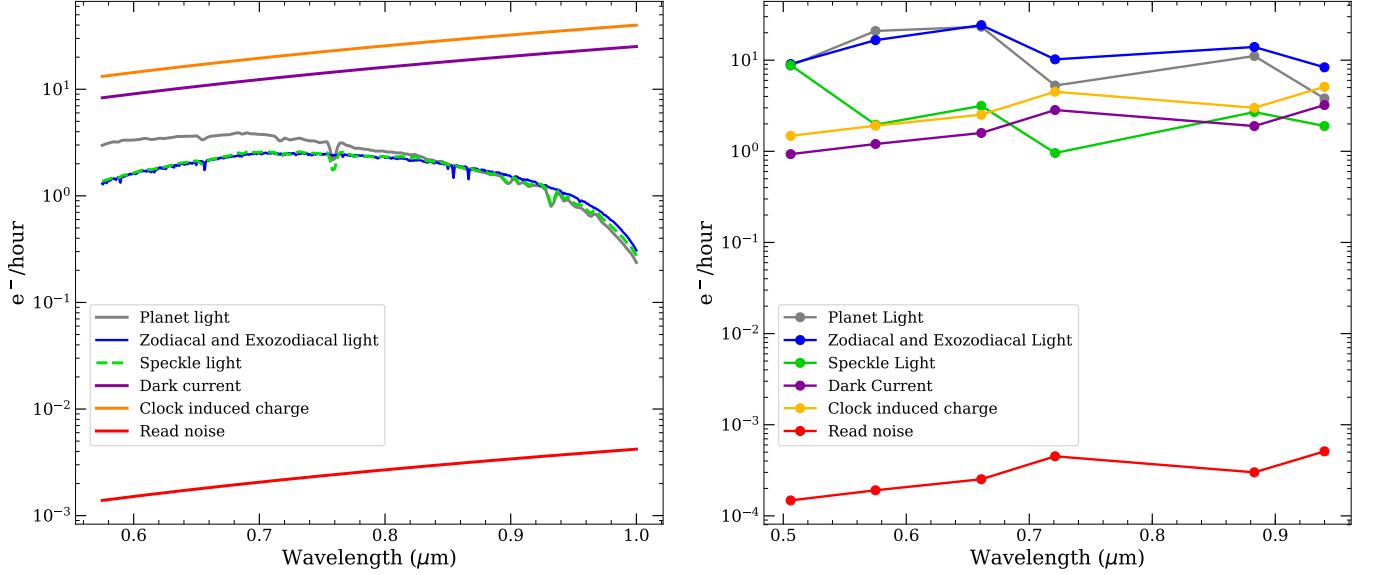


Figure 22. Representative comparison of the count rates for all sources contributing to signal and noise calculations in the IFS (**left**) and imaging (**right**) modes of WFIRST-CGI. In both cases we have assumed a fiducial planet-star system approximating the Jupiter-Sun system: a 4.83 magnitude G0V primary and a $1 R_J$ planet orbiting at a separation of 5 AU, all observed from a distance of 11 pc. To more clearly show the dependence of noise sources with wavelength, we assume a gray planet and phase function such that $\Phi(\alpha)A_g(\lambda) = 0.25$. Note that, in the imaging mode, dots mark the center of each bandpass; we have simply connected them to guide the eye. Spectral dependencies (particularly the dip at $\sim 0.76 \mu\text{m}$) in the planet light, speckle light, and zodiacal light arise from the G0V spectra, taken from the Bruzual-Persson-Gunn-Stryker Stellar Spectrophotometric Atlas, which is distributed with the HST Synphot software^a. Zodiacal count rates also make use of the solar spectra of Kurucz (2005). The sharp kink in the planet, speckle, and zodiacal count rates occurring at $\sim 0.7 \mu\text{m}$ and the subsequent decline in count rate, are consequences of our piece-wise expression for η , eq. (A1). In contrast, the dark current and clock-induced charge count rates rise with wavelength as the ratio $\frac{\lambda}{D}$ increases and more pixels are included in the PSF region. In imaging mode, dark current and clock-induced charge count rates fall below planet light and zodiacal light due to lower resolution and because the imaging signal region incorporates ~ 3 times fewer pixels than the IFS signal region. ^a<http://pysynphot.readthedocs.io/en/latest/appendixa.html>

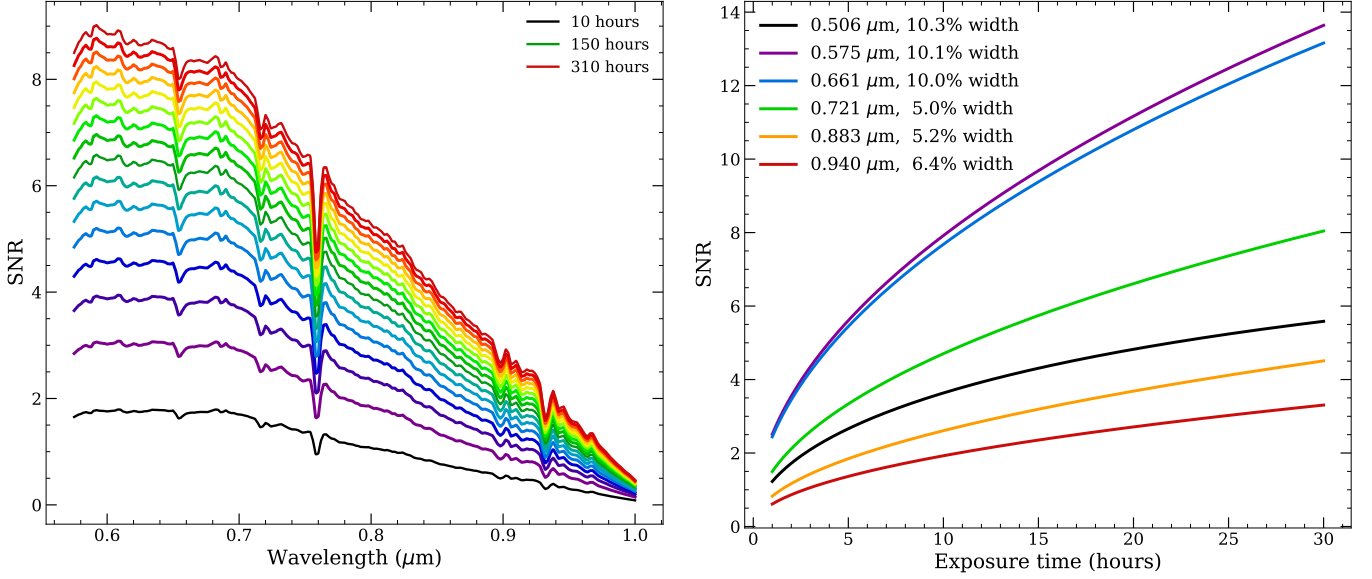


Figure 23. **Left** panel shows SNR achieved with the IFS for on-target exposure times varying from 10 to 310 hours in 20 hour intervals. At longer wavelengths where larger PSFs include more pixels (thus including more clock-induced charge and dark current noise), and the quantum efficiency has dropped (reducing the planet signal), the SNR is low even for the longest allowable exposure time of 300 hours. We have assumed the same fiducial system as Figure 22: a Sun-like star with a Jupiter-sized planet orbiting at 5 AU observed from a distance of 11 parsecs. We assume a gray planet and phase function such that $\Phi(\alpha)A_g(\lambda) = 0.25$ in order to emphasize the wavelength dependence of coronagraph performance, rather than the wavelength dependence of the planet atmosphere. Similar to Figure 22, spectral features seen in the IFS performance originate from the assumed primary star and solar spectrum. **Right** panel shows the scaling of SNR with exposure time for the six WFIRST-CGI imaging bands using the same fiducial system. As is implied by eq. (11), SNR scales approximately with the inverse square root of exposure time (the same is true of the IFS, but this is less clear in the form we have plotted it). The primary differences between the SNR calculations for images and spectra are the use of the HLC rather than the SPC, the incorporation of an “excess noise factor” representing the stochasticity of the electron multiplication gain process, and the significantly smaller number of pixels involved in the signal region. Typically, imaging requires an order of magnitude shorter exposure time to achieve any given SNR . For many planet-star systems, the 0.506- μm imaging band would obtain an SNR closer to those of the 0.575- μm and 0.661- μm filters, but, for this fiducial system, the 0.506- μm band falls in an area of poor coronagraph performance (see purple dashed line and solid gray line in Figure 1).

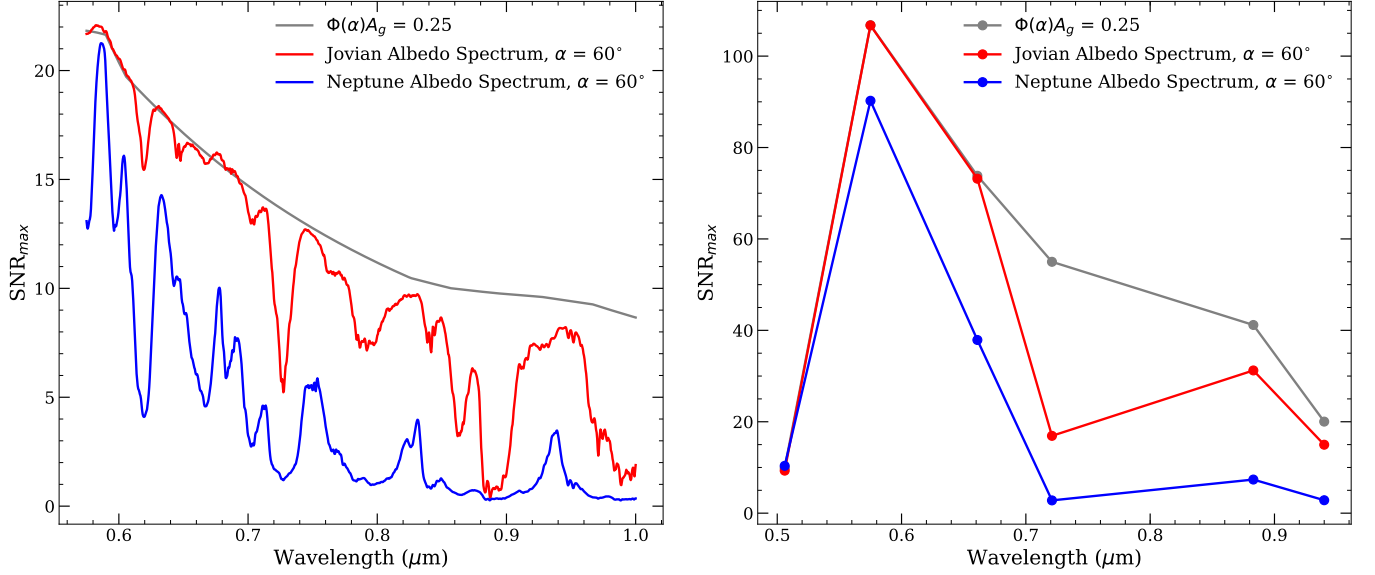


Figure 24. Comparison of SNR_{max} as discussed in eq. (12) for three different geometric albedo spectra across the wavelengths in which WFIRST-CGI will observe. The **left** panel shows the IFS capabilities, the **right** panel shows the imaging capabilities with the six band centers marked by dots. In both cases, we have assumed our fiducial system: a 4.83 V-magnitude G0V type host star with a $1.0 R_J$ planet orbiting at a separation of 5 AU, all observed from a distance of 11 pc. The blue and red lines correspond to the observed geometric albedo spectra of Neptune and Jupiter, respectively (Karkoschka, 1994) observed at $\alpha = 60^\circ$, assuming an empirically measured phase function (Mayorga 2016). The gray line corresponds to a gray geometric albedo spectrum such that $\Phi(\alpha)A_g(\lambda) = 0.25$. A similar overall pattern is seen for both imaging and spectra, but achievable SNR levels are an order of magnitude higher for the imaging bands, except the $0.506\text{-}\mu\text{m}$ band, which barely falls in the coronagraph’s functioning working angles. The IFS SNR_{max} values show that it may not be possible to attain high signal-to-noise ratio measurements at the bottom of deep absorption features, regardless of integration time.

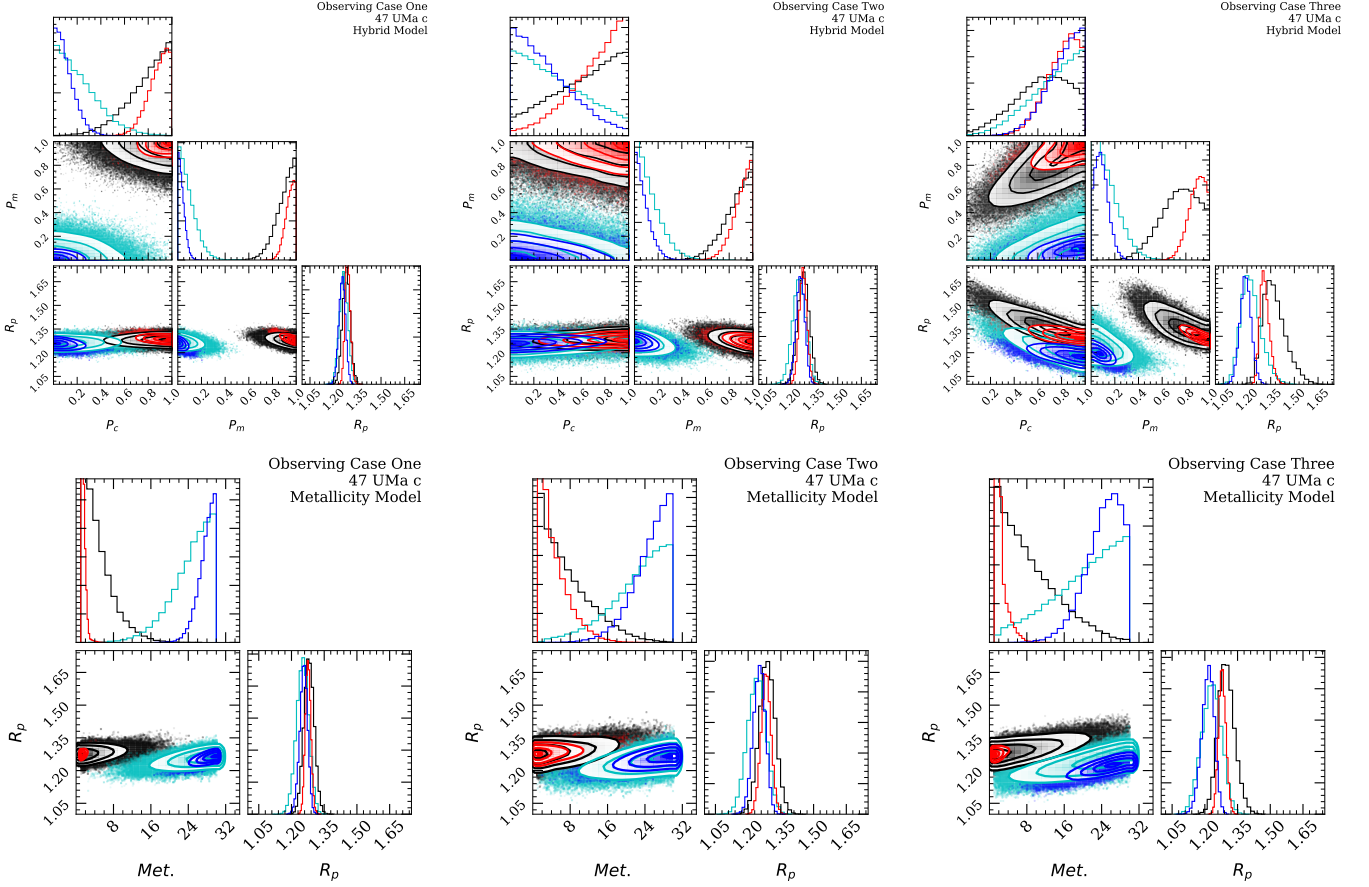


Figure 25. Triangle plots showing the MCMC sampling of the posterior distributions of the Hybrid model parameters (**top row**) and the *CoolTLusty* model parameters (**bottom row**) for the three observing cases (**left:** case one, **center:** case two, **right:** case three, cases defined in §5.2), carried out for a planet-star system with the inferred characteristics of 47 UMa c listed in Table 2. The top row is similar to Figure 14, with the fully Jovian-like parameterization, $P_c=1.00$, $P_m=1.00$, shown in red (285-hour exposure/24-hour exposure for cases one and three/case two respectively) and black (95-hour exposure/10-hour exposure). The fully Neptune-like parameterization, $P_c=0.00$, $P_m=0.00$, is shown in blue (285-hour exposure/24-hour exposure) and in cyan (95-hour exposure/10-hour exposure). The bottom row is similar to Figure 17, with a solar-metallicity parameterization shown in red (285-hour exposure/24-hour exposure) and black (95-hour exposure/10-hour exposure). A 30-times solar metallicity parameterization is shown in blue (285-hour exposure/24-hour exposure) and in cyan (95-hour exposure/10-hour exposure). Contours mark the 0.5-sigma, 1-sigma, 2-sigma and 2.5-sigma regions, with points outside these regions represented as dots. Like our fiducial system, it is assumed that 47 UMa c is observed at an orbital phase angle of 60° and exhibits the empirical Jovian phase curve reported by Mayorga et al. 2016. 47 UMa c attains a higher SNR than our fiducial system at these exposure times, so R_p , metallicity, and P_m are better constrained. Even P_c is significantly better constrained, since the $0.506\text{-}\mu\text{m}$ imaging band does not fall at a working angle with degraded coronagraph performance as it does for the fiducial case. Not surprisingly, observing case one, with the most wavelength coverage and largest aggregate observing times, provides the strongest constraints on model parameters. 47 UMa c is inferred to have a larger radius than Jupiter and is at a separation of only 3.57 AU. These qualities make it a stronger candidate for WFIRST-CGI characterization than a Jupiter-Sun twin system.

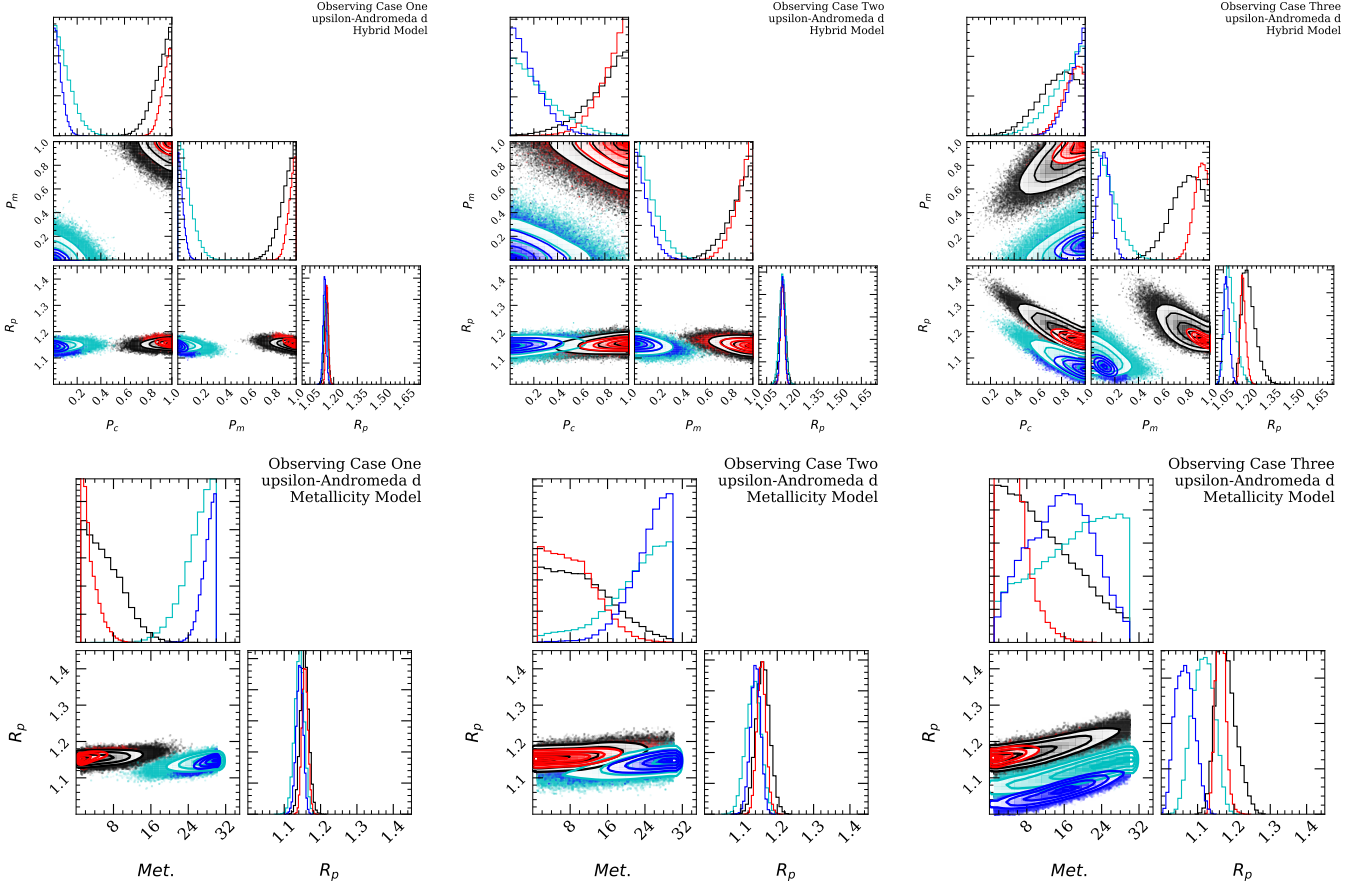


Figure 26. Triangle plots showing the MCMC sampling of the posterior distributions of the Hybrid model parameters (**top row**) and the *CoolTLusty* model parameters (**bottom row**) for the three observing cases (**left**: case one, **center**: case two, **right**: case three), all carried out for a planet-star system with the inferred characteristics of Upsilon And d listed in Table 2. This plot is similar to Figure 25, except it is assumed that Upsilon And d is observed at a phase angle of 90° to minimize the wavelength coverage which falls interior to the inner working angle of the coronagraph. Upsilon And d has a semi-major axis of only 2.52, and is nearer by than 47 UMa c. In the regions of the spectrum where it falls exterior to the inner working angle of the coronagraph, it therefore attains a higher *SNR* than 47 UMa c. This higher *SNR*, but more limited wavelength coverage together result in similar *CoolTLusty* parameter errors. The hybrid model does better than 47 UMa c, presumably since the short-wavelength imaging bands are unaffected by the inner working angle of the coronagraph and provide a better constraint on P_c .

REFERENCES

- Foreman-Mackey, D. 2016, *The Journal of Open Source Software*, 2016,
- Nemati, B., Stahl, M. T., Stahl, H. P., & Shaklan, S. B. 2017, *Society of Photo-Optical Instrumentation Engineers (SPIE) Conference Series*, 10398, 103980G
- Savransky, D., Kasdin, N. J., & Cady, E. 2010, *PASP*, 122, 401
- Brown, R. A., & Soummer, R. 2010, *ApJ*, 715, 122
- Agol, E. 2007, *MNRAS*, 374, 1271
- Turnbull, M. C., Glassman, T., Roberge, A., et al. 2012, *PASP*, 124, 418
- Savransky, D., & Garrett, D. 2016, *Journal of Astronomical Telescopes, Instruments, and Systems*, 2, 011006
- Garrett, D., Savransky, D., & Macintosh, B. 2017, *AJ*, 154, 47
- Cady, E., Prada, C. M., An, X., et al. 2016, *Journal of Astronomical Telescopes, Instruments, and Systems*, 2, 011004
- Carlotti, A., Vanderbei, R., & Kasdin, N. J. 2011, *Optics Express*, 19, 26796
- Soummer, R. 2005, *ApJL*, 618, L161
- Kasdin, N. J., Vanderbei, R. J., Spergel, D. N., & Littman, M. G. 2003, *ApJ*, 582, 1147
- Harding, L. K., Demers, R. T., Hoenk, M., et al. 2016, *Journal of Astronomical Telescopes, Instruments, and Systems*, 2, 011007
- Denvir, D. J., & Conroy, E. 2003, *Proc. SPIE*, 4796, 164
- Saxena, P., Rizzo, M. J., Mejia Prada, C., et al. 2017, *arXiv:1707.07779*
- Macintosh, B., Graham, J., Palmer, D., et al. 2006, *Proc. SPIE*, 6272, 62720L
- Mesa, D., Gratton, R., Zurlo, A., et al. 2015, *A&A*, 576, A121
- Zimmerman, N. T., Riggs, A. J. E., Kasdin, N. J., Carlotti, A., & Vanderbei, R. J. 2015, *Proc. SPIE*, 9605, 96050A
- Give'On, A. 2009, *Proc. SPIE*, 7440, 74400D
- Rizzo, M. J., Groff, T. D., Zimmerman, N. T., et al. 2017, *arXiv:1709.09248*
- Spergel, D., Gehrels, N., Breckinridge, J., et al. 2013, *arXiv:1305.5422*
- Zhao, F. 2014, *Proc. SPIE*, 9143, 91430O
- Noecker, M. C., Zhao, F., Demers, R., et al. 2016, *Journal of Astronomical Telescopes, Instruments, and Systems*, 2, 011001
- Mallama, A. 2012, *Icarus*, 218, 56
- Schmude, R. W., Jr., Baker, R. E., Fox, J., Krobusek, B. A., & Mallama, A. 2015, *arXiv:1510.04175*
- Schmude, R. W., Jr., Baker, R. E., Fox, J., et al. 2016, *arXiv:1604.00518*
- Yurchenko, S. N., & Tennyson, J. 2014, *MNRAS*, 440, 1649
- Hubeny, I., & Lanz, T. 1995, *ApJ*, 439, 875
- Burrows, A., Sudarsky, D., & Hubeny, I. 2006, *ApJ*, 650, 1140
- Khare, B. N., Sagan, C., Arakawa, E. T., et al. 1984, *Icarus*, 60, 127
- Karkoschka, E. 1998, *Icarus*, 133, 134
- Burrows, A., & Sharp, C. M. 1999, *ApJ*, 512, 843
- Sudarsky, D., Burrows, A., & Pinto, P. 2000, *ApJ*, 538, 885
- Greco, J. P., & Burrows, A. 2015, *ApJ*, 808, 172
- Sudarsky, D., Burrows, A., & Hubeny, I. 2003, *ApJ*, 588, 1121
- Madhusudhan, N., & Burrows, A. 2012, *ApJ*, 747, 25
- Stam, D. M., Hovenier, J. W., & Waters, L. B. F. M. 2004, *A&A*, 428, 663
- Seager, S., Whitney, B. A., & Sasselov, D. D. 2000, *ApJ*, 540, 504
- Seager, S., & Sasselov, D. D. 1998, *ApJL*, 502, L157
- van de Hulst, H. C. 1981, *New York: Dover*, 1981,
- van de Hulst, H. C. 1974, *A&A*, 35, 209
- Horak, H. G. 1950, *ApJ*, 112, 445
- Russell, H. N. 1916, *ApJ*, 43, 173
- Dyudina, U. A., Zhang, X., Li, L., et al. 2016, *AAS/Division for Planetary Sciences Meeting Abstracts #48*, 48, 202.08
- Mayorga, L., Jackiewicz, J., Rages, K., et al. 2016, *AAS/Division for Planetary Sciences Meeting Abstracts #48*, 48, 202.07
- Sudarsky, D., Burrows, A., Hubeny, I., & Li, A. 2005, *ApJ*, 627, 520
- Burrows, A., Sudarsky, D., & Hubeny, I. 2004, *ApJ*, 609, 407
- Burrows, A. 2014, *arXiv:1412.6097*
- Dyudina, U. A., Sackett, P. D., Bayliss, D. D. R., et al. 2005, *ApJ*, 618, 973
- Karkoschka, E. 1994, *Icarus*, 111, 174
- Cahoy, K. L., Marley, M. S., & Fortney, J. J. 2010, *ApJ*, 724, 189

- Sromovsky, L. A., Baines, K. H., Fry, P. M., & Carlson, R. W. 2017, *Icarus*, 291, 232
- Nayak, M., Lupu, R., Marley, M. S., et al. 2017, *PASP*, 129, 034401
- Lupu, R. E., Marley, M. S., Lewis, N., et al. 2016, *AJ*, 152, 217
- Krist, J., Nemati, B., & Mennesson, B. 2016, *Journal of Astronomical Telescopes, Instruments, and Systems*, 2, 011003
- Robinson, T. D., Stapelfeldt, K. R., & Marley, M. S. 2016, *PASP*, 128, 025003
- Foreman-Mackey, D., Hogg, D. W., Lang, D., & Goodman, J. 2013, *PASP*, 125, 306
- Trauger, J., Moody, D., Krist, J., & Gordon, B. 2016, *Journal of Astronomical Telescopes, Instruments, and Systems*, 2, 011013
- Balasubramanian, K., White, V., Yee, K., et al. 2016, *Journal of Astronomical Telescopes, Instruments, and Systems*, 2, 011005
- Ygouf, M., Pueyo, L., Soummer, R., et al. 2015, *Proc. SPIE*, 9605, 96050S
- Nemati, B. 2014, *Proc. SPIE*, 9143, 91430Q
- Stark, C. C., Roberge, A., Mandell, A., & Robinson, T. D. 2014, *ApJ*, 795, 122
- Levasseur-Regourd, A. C., & Dumont, R. 1980, *A&A*, 84, 277
- Traub, W. A., & Oppenheimer, B. R. 2010, *Exoplanets*, 111
- Traub, W. A., Breckinridge, J., Greene, T. P., et al. 2016, *Journal of Astronomical Telescopes, Instruments, and Systems*, 2, 011020
- Daemgen, S., Todorov, K., Quanz, S. P., et al. 2017, *A&A*, 608, A71
- Lendl, M., Cubillos, P. E., Hagelberg, J., et al. 2017, *A&A*, 606, A18
- Oklopčić, A., Hirata, C. M., & Heng, K. 2017, *ApJ*, 846, 91
- Mallama, A., Krobusek, B., & Pavlov, H. 2017, *Icarus*, 282, 19
- Kurucz, R. L. 2005, *Memorie della Societa Astronomica Italiana Supplementi*, 8, 189
- Thorngren, D. P., Fortney, J. J., Murray-Clay, R. A., & Lopez, E. D. 2016, *ApJ*, 831, 64
- Pinhas, A., & Madhusudhan, N. 2017, *MNRAS*, 471, 4355
- Butler, R. P., Vogt, S. S., Laughlin, G., et al. 2017, *VizieR Online Data Catalog*, 515,
- Butkevich, A. G. 2017, *arXiv:1709.00290*
- Zakharov, A. 2016, 41st COSPAR Scientific Assembly, 41,
- Ngo, H. 2017, *American Astronomical Society Meeting Abstracts*, 229, 303.01
- Xie, J.-W., Dong, S., Zhu, Z., et al. 2016, *Proceedings of the National Academy of Science*, 113, 11431
- Ranalli, P., Hobbs, D., & Lindegren, L. 2017, *arXiv:1704.02493*
- Shporer, A., Zhou, G., Vanderburg, A., et al. 2017, *ApJL*, 847, L18
- Marley, M. S., Gelino, C., Stephens, D., Lunine, J. I., & Freedman, R. 1999, *ApJ*, 513, 879
- Skemer, A. J., Morley, C. V., Zimmerman, N. T., et al. 2016, *ApJ*, 817, 166
- Hu, R., Demory, B.-O., Seager, S., Lewis, N., & Showman, A. P. 2015, *ApJ*, 802, 51
- Pace, G., 1971, NASA technical report: “UBV: Subroutine to Compute Photometric Magnitudes of the Planets and Their Satellites”
- Goodman, J., & Weare, J. 2010, *Communications in Applied Mathematics and Computational Science*, Vol. 5, No. 1, p. 65-80, 2010, 5, 65